Research Article Vol. 63, No. 36 / 20 December 2024 / Applied Optics 9315

applied optics

Performance of the ultraviolet laser transmitter during ESA's Doppler wind lidar mission Aeolus

Oliver Lux,[1,*] Christian Lemmerz,[1] Valeria De Sanctis,[2] Paolo Bravetti,[3,4] Denny Wernham,[4] Trismono Candra Krisna,[4] Tommaso Parrinello,[5] and Oliver Reitebuch[1]

[1]German Aerospace Center (Deutsches Zentrum für Luft- und Raumfahrt), Institute of Atmospheric Physics, 82234 Oberpfaffenhofen, Germany
[2]Leonardo S.p.A., Via Industria, 4, 00040 Pomezia RM, Italy
[3]Airbus Italia S.p.A., Via dei Luxardo, 22-24, 00156 Rome, Italy
[4]European Space Agency-ESTEC, Keplerlaan 1, Noordwijk NL-2201AZ, The Netherlands
[5]European Space Agency-ESRIN, Largo Galileo Galilei, 1, 00044 Frascati RM, Italy
*oliver.lux@dlr.de

Received 10 October 2024; revised 19 November 2024; accepted 19 November 2024; posted 19 November 2024; published 13 December 2024

The European Space Agency's Aeolus mission was a groundbreaking achievement in Earth observation and space laser technology. Over its nearly five-year lifetime, the space-borne Doppler wind lidar instrument onboard Aeolus utilized two redundant ultraviolet (UV) lasers to measure atmospheric wind profiles globally, significantly enhancing the accuracy of numerical weather predictions. The laser transmitters were frequency-tripled, injection-seeded Nd:YAG systems, configured in a master oscillator power amplifier arrangement, generating single-longitudinal-mode pulses at 354.8 nm with a pulse duration of around 20 ns. Across the mission, both transmitters together generated more than $7 \cdot 10^9$ UV laser pulses. The performance of both the nominal and redundant lasers was optimized and stabilized by carefully regulating their thermal environment, which influenced the laser energy depending on the emission frequency. At the optimum laser bench temperature, both lasers delivered stable UV output with pulse energies exceeding 60 mJ. The energy of the second laser, operational from June 2019 to October 2022, was further enhanced to over 100 mJ through step-wise increases in master oscillator pump power and adjustments of the amplifier pump phase. Following the mission's operational phase, a series of tests was conducted close before the mission end-of-life (EOL) to address instrument-related questions. During these EOL activities, the laser power was boosted to more than 150 mJ for 20 days and even over 180 mJ for 33 h, setting a new, to the best of our knowledge, record for a UV space laser. Additionally, the frequency stability of the two lasers was evaluated, revealing detrimental impact from micro-vibrations caused by the satellite's reaction wheels. EOL tests showed that adjustments to the master oscillator cavity control sequence significantly mitigated these effects, improving the laser frequency stability by a factor of two to better than 7 MHz (standard deviation over the period of one wind observation of 12 s). This paper provides a comprehensive overview of the ALADIN laser transmitters' architecture, operation, and performance during the Aeolus mission from 2018 to 2023, with a focus on energy and frequency stability improvements relevant to current and future space lidar missions such as EarthCARE and Aeolus-2.

https://doi.org/10.1364/AO.544577

1. INTRODUCTION

The European Space Agency's (ESA) Aeolus mission was the world's first satellite mission dedicated to measuring global wind profiles. Launched on August 22, 2018, the mission successfully concluded on July 5, 2023, surpassing its intended 39-month nominal lifetime (including a 3-month commissioning phase) by 20 months, before the satellite re-entered Earth's atmosphere on July 28, 2023. Its single payload, the Atmospheric Laser Doppler Instrument (ALADIN), marked the debut of both European lidar technology and Doppler wind lidar in space [1,2]. Serving as an Earth Explorer mission, Aeolus was initially conceived as a technology demonstrator for future operational wind lidar missions. However, within two years of launch, the global wind measurements were operationally used in numerical weather prediction (NWP) models by major weather services, including the German Weather Service [3], Météo France [4], the UK Met Office [5], and the European Centre for Medium-Range Weather Forecasts (ECMWF). The wind profiles measured by Aeolus improved global NWP forecasts by

a magnitude comparable to several other important operational satellite observing systems [6]. This was a remarkable feat for a demonstrator mission, especially considering Aeolus accounted for fewer than 0.5% of the observations assimilated by ECMWF [7]. Furthermore, the wind data have been utilized for a variety of scientific studies, including investigations of global-scale tropical waves [8], analyses of extreme dynamical events in the stratosphere [9], and correlations between aerosol optical properties and wind fields over oceans [10]. In addition to wind observations, ALADIN provided aerosol and cloud backscatter as well as extinction profiles, independently determined using high-spectral-resolution lidar (HSRL) for the first time from space [11,12].

Since the 1990s, a diverse array of space-borne lidars has been developed to collect data on various atmospheric parameters on a global scale. The Lidar In-space Technology Experiment (LITE) aboard the Space Shuttle Discovery in 1994 pioneered the use of a space-borne lidar for atmospheric research [13]. The Ice, Cloud and Land Elevation Satellite (ICESat) mission, active from 2003 to 2009, employed the Geoscience Laser Altimeter System (GLAS) [14]. Since late 2018, the ICESat–2 mission has utilized the Advanced Topographic Laser Altimeter System to measure sea ice freeboard and ice sheet elevation [15]. Another notable breakthrough came with the launch of the Cloud-Aerosol Lidar and Infrared Pathfinder Satellite Observation (CALIPSO) in 2006, carrying the Cloud-Aerosol Lidar with Orthogonal Polarization (CALIOP) [16]. It was the first lidar for aerosol and cloud observations from space, which was operational over 17 years until the end of the mission in August 2023. From 2015 to 2018, the Cloud-Aerosol Transport System (CATS) aboard the International Space Station enabled the collection of cloud and aerosol profiles [17]. In 2022, the atmospheric environment monitoring satellite Daqi-1 was launched, carrying the Aerosol and Carbon Detection Lidar (ACDL). The ACDL features a two-wavelength HSRL for globally profiling aerosol and cloud optical properties, along with an integrated-path differential absorption lidar for measuring carbon dioxide column concentrations [18]. Finally, ESA's sixth Earth Explorer mission, EarthCARE (Earth Clouds, Aerosol and Radiation Explorer), was launched on May 28, 2024, in collaboration with the Japan Aerospace Exploration Agency (JAXA). It includes, among other instruments, the Atmospheric Lidar (ATLID), an HSRL operating at 355 nm to measure cloud and aerosol profiles with a vertical resolution of $\approx$ 100 m using laser transmitters similar to those embarked on ALADIN [19].

Most of the aforementioned space-borne lidar instruments deployed lasers emitting in the visible and infrared (IR) spectral regions. Prior to the launch of Aeolus and EarthCARE, only LITE operated an ultraviolet (UV) laser in space, for about 50 h [13]. The UV laser foreseen for the CATS mission was not operable due to an unexpected failure in the laser optical path [20]. In general, UV lasers are challenging to operate, especially in vacuum environments, due to the phenomena of laser-induced damage (LID) and laser-induced contamination (LIC). The high energy of UV photons can cause rapid degradation of optical components through mechanisms like material ablation, dielectric breakdown, or photo-chemical reactions. In vacuum, the absence of atmospheric gases means that contaminants on optical surfaces, such as hydrocarbons or outgassed materials, are not easily removed. Instead, the outgassed products can interact with the laser on the surface of the optics resulting in highly absorbing deposits. This cycle of damage and contamination can drastically shorten the lifespan and reliability of UV laser systems in such environments [21].

In addition to the difference in emission wavelength, the requirements for spectral laser properties in previous space missions were much less stringent compared to those for Aeolus, as the instruments primarily operated as Mie backscatter or polarization lidars measuring aerosol and cloud returns. In contrast, Aeolus relied on the measurement of Doppler frequency shifts as small as a few MHz, necessitating laser frequency stability of the same order. Therefore, the long-term operation of high-power, frequency-stable lasers represents a major achievement in the field of space-based lasers. This work details the methods used to achieve this milestone, provides an overview of the lasers' performance over the nearly five-year mission, and discusses the limitations encountered.

The structure of the paper is as follows: in Section 2, we elaborate on the architecture of the ALADIN laser transmitters. Section 2.A summarizes the on-ground tests prior to launch, while Section 2.B outlines the methods to mitigate laser-induced contamination and damage to enable the long-term laser operation. The in-orbit performance in terms of the UV output energy is discussed in Section 3 with a focus on its sensitivity to thermal variations of the laser bench (Section 3.A). Special operations conducted during the mission lifetime to study and optimize the laser properties are covered in Section 3.B, while Section 3.C addresses the laser beam profile. Final tests performed at the end of mission are presented in Section 3.D, followed by an overview of interruptions of the laser operation in Section 3.E. In Section 3.F the results obtained in the on-ground laser test facility are presented. Section 4 examines the frequency stability of the ALADIN lasers, detailing the detrimental impact of micro-vibrations (Section 4.A) as well as stability improvements during dedicated in-orbit tests at the end of the mission (Section 4.B). The paper closes with a summary and outlook on other space missions using UV lasers in Section 5. A list of abbreviations is provided in Supplement 1.

2. LASER DESIGN

ALADIN was equipped with two fully redundant laser transmitters, denoted as flight models (FM) A and B, which were switchable by means of a flip-flop mechanism (FFM). Both transmitters were realized as diode-pumped Nd:YAG lasers in a master oscillator power amplifier (MOPA) configuration that were frequency-tripled to 354.8 nm emission wavelength [22–26]. This configuration, also referred to as the power laser head (PLH), comprised five main stages, as depicted in Fig. 1. In the first stage, the narrowband seed radiation generated from a Nd:YAG non-planar ring oscillator (NPRO), the so-called reference laser head (RLH), was fiber-coupled into the folded cavity of the 80 cm long *Q*-switched master oscillator (MO). The NPRO itself was tunable and frequency-locked to a second reference NPRO that was stabilized to an ultra-low-expansion cavity resonance for enhanced frequency stability [27–29]. The length of the MO cavity was actively adjusted with a piezo

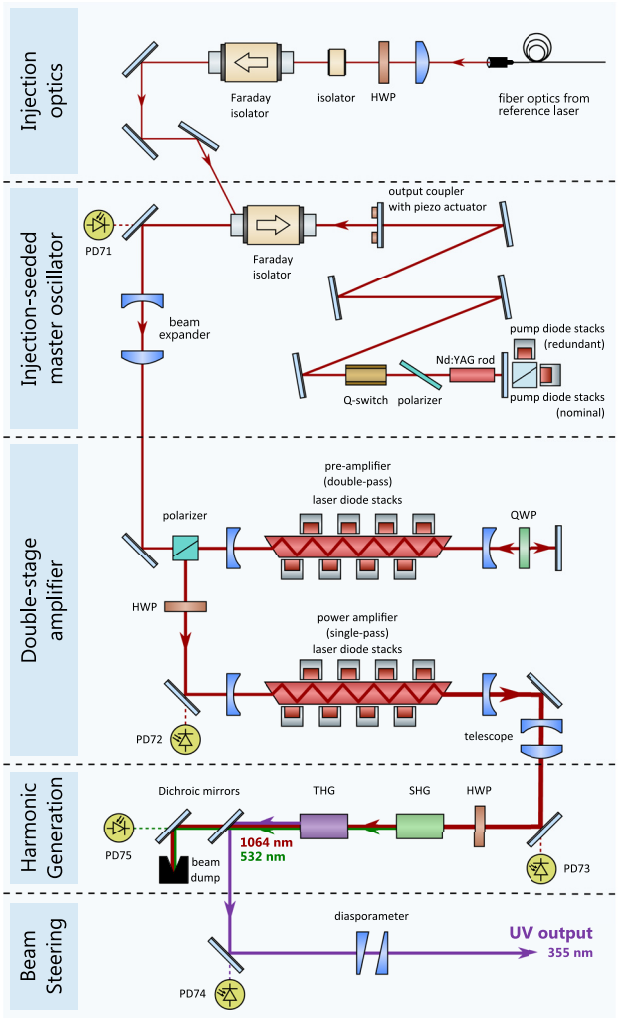

Fig. 1. Simplified schematic of the ALADIN laser transmitter. HWP, half-wave plate; QWP, quarter-wave plate; SHG/THG, second/third-harmonic generator; PD, photodiode.

actuator for each laser pulse to ensure single-longitudinal-mode operation [23].

The cavity control method was based on the ramp-hold-fire technique [30], which involves detecting cavity resonances of the injected seed radiation while adjusting the cavity length using a piezo actuator that is attached to the output coupling mirror of the MO cavity. The *Q*-switch is triggered when the resonance position of the actuator is detected, as detailed in Section 4.B. Implementing this technique in the MO allowed for a cavity length precision of better than a few nanometers. However, it had the drawback of a millisecond-range delay between cavity resonance detection and laser pulse emission [31].

The output pulses from the MO, with pulse repetition frequency of 50.5 Hz and pulse energy ranging from 5 to 10 mJ, were subsequently amplified in two stages. The first stage, also referred to as pre-amplifier (PreAMP), utilized a double-pass configuration, while the second stage, the power amplifier (AMP), operated in single-pass mode. Both amplifiers employed side-pumped and conductively cooled Nd:YAG zigzag slabs, boosting the energy of the IR laser pulses to over 250 mJ. The amplified IR beam then passed through a higher-harmonic-generation (HHG) stage, which included a set of nonlinear lithium triborate (LBO) crystals, converting the IR pulses to UV output with a total conversion efficiency of 25% to 50%, depending on the intensities within the crystals, and yielding UV pulse energies exceeding 60 mJ. Finally, the UV beam's pointing was adjusted by a diasporameter to ensure precise alignment along the emission path of the ALADIN instrument.

The laser pulse duration was approximately 20 ns (full width at half maximum, FWHM), corresponding to a Fourier-transform limit of the pulse spectral width (FWHM) of $\Delta\nu \geq 0.441/\Delta\tau \approx 22$ MHz for a Gaussian-shaped pulse and $\Delta\nu \geq 0.142/\Delta\tau \approx 7$ MHz for a Lorentzian-shaped pulse. However, heterodyne measurements of the ALADIN Airborne Demonstrator (A2D) laser transmitter, which is based on a similar MOPA configuration with comparable specifications, revealed that the actual linewidth was approximately twice the Fourier-transform limit [32]. This spectral broadening is attributed to a frequency chirp, most likely caused by changes in population inversion during pulse evolution. As the same effect is assumed for the ALADIN lasers, the spectral width is expected to be larger than the Fourier-transform limit, but still below 50 MHz. A more detailed analysis of the laser linewidth, including an approximation of Gaussian and Lorentzian contributions to the line shape, is part of a forthcoming publication on the spectral performance of the ALADIN receiver. The main parameters of the two ALADIN lasers, as obtained in-orbit, are summarized in Table 1.

Both the PLH and RLH were supplied and controlled by a transmitter laser electronics (TLE) unit. The TLE was organized into two main sections: the power section, which contained the laser diode power supplies for the MO and amplifiers, and the interface and control section, which housed several boards dedicated to commanding and controlling the PLH and RLH operations, and interfacing with the Instrument ALADIN Control and Data Management (ACDM) unit.

The UV beam from one of the two switchable lasers was directed through a configuration of transmit-receive optics (TRO), arranged in a sealed cavity separated from the PLH, where its diameter was expanded from 6.1 mm (86% encircled energy, EE) to approximately 21 mm using a beam expander. Moreover, a small portion (0.5%) of the light was transmitted through a beam splitter within the TRO and, after being attenuated, guided to the instrument field stop and receiver channels. This portion is referred to as the internal reference (INT) path signal and was utilized for determining the emitted laser frequency and for calibrating the frequency-dependent transmission of the receiver spectrometers. In contrast to ALADIN, where the INT signal was delivered to the spectrometers on a free optical path, the A2D configuration used multimode fibers, requiring a fiber scrambler to reduce speckle noise and improve frequency measurement precision [33].

The powerful laser output reflected from the beam splitter was directed into the atmosphere by a Cassegrain-type telescope, which was used in a monostatic configuration, i.e., signal emission and reception were realized via the same primary and secondary mirrors. The former had a diameter of 1.5 m and a magnification factor of 41.7, thereby further enlarging the laser

Table 1. Selected In-Orbit Parameters of the ALADIN Laser Transmitters Operating at 354.8 nm Wavelength

Parameter	Value
Type	Frequency-tripled Nd:YAG
Laser cooling	Conductively via cold-plate
Laser wavelength (vacuum)	354.8 nm
Repetition rate	50.5 Hz
Pulse energy (on-ground scaling factors: FM-A: 0.77; FM-B: 0.94)	FM-A: 40 to 70 mJ; FM-B: 60 to 100 mJ (>150 mJ over 20 days) (>180 mJ over 33 h)
Energy stability (standard deviation over 1 h)	1%–2%
Pulse width (FWHM)	≈ 20 ns
Spectral width (FWHM)	<50 MHz
Frequency stability (standard deviation over 540 pulses, 12 s)	<12 MHz (<7 MHz at optimized cavity control setting)
Beam diameter (86% encircled energy, near-field)	<6.1 mm (horizontal) <4.7 mm (vertical)
Beam divergence (full angle, 86% encircled energy)	<700 μrad
Transmitter laser electronics efficiency	80%
Laser diode electrical-to-optical efficiency	45%–50%
Pumping efficiency (MO to AMP)	10%–20%
Frequency conversion efficiency	25%–30% (up to 50% during EOL tests)
Operation time in space	FM-A: 15 months; FM-B: 41 months
Total number of laser pulses	FM-A: 1.8 Gigashots; FM-B: 5.3 Gigashots

beam to a diameter of ≈ 0.9 m. The laser divergence ranged from 18 to 20 μrad (86% EE) at the exit of the ALADIN telescope. Consequently, the laser beam's footprint on the Earth's surface, from a satellite altitude of 320 km and an off-nadir angle of 37.7°, spanned approximately 8 m. Upon its return, the backscattered signal collected by the same telescope passed through the field stop with a diameter of merely 88 μm. As a result, the receiver's field of view was constrained to about 18 μrad, thereby reducing the influence of solar background radiation and accommodating the high angular sensitivity of the spectrometers.

The ALADIN receiver consisted of two complementary channels with different types of spectrometers, each employed to determine the Doppler frequency shift that was introduced by the interaction of the light pulses with atmospheric molecules and particles moving with the ambient wind. One channel was specified for analyzing the narrowband (FWHM ≈ 50 MHz) Mie backscatter originating from particles like clouds and aerosols by means of a Fizeau interferometer. The other channel addressed the broadband Rayleigh–Brillouin molecular backscatter (FWHM ≈ 3.8 GHz at 355 nm and 293 K) using Fabry–Pérot interferometers. Charge-coupled device detectors were utilized in both channels to capture the Mie and Rayleigh backscatter signals. A detailed description of the design and functionality of the ALADIN receiver channels and detectors is provided in [26,34–36].

To fit within the available volume of approximately 30 liters, the optics were arranged on two optical benches: the upper optical bench contained all active components (master oscillator and amplifiers), while the lower optical bench carried the HHG stage, beam-shaping optics, and optical isolators (Fig. 2). The active components were conductively cooled through a

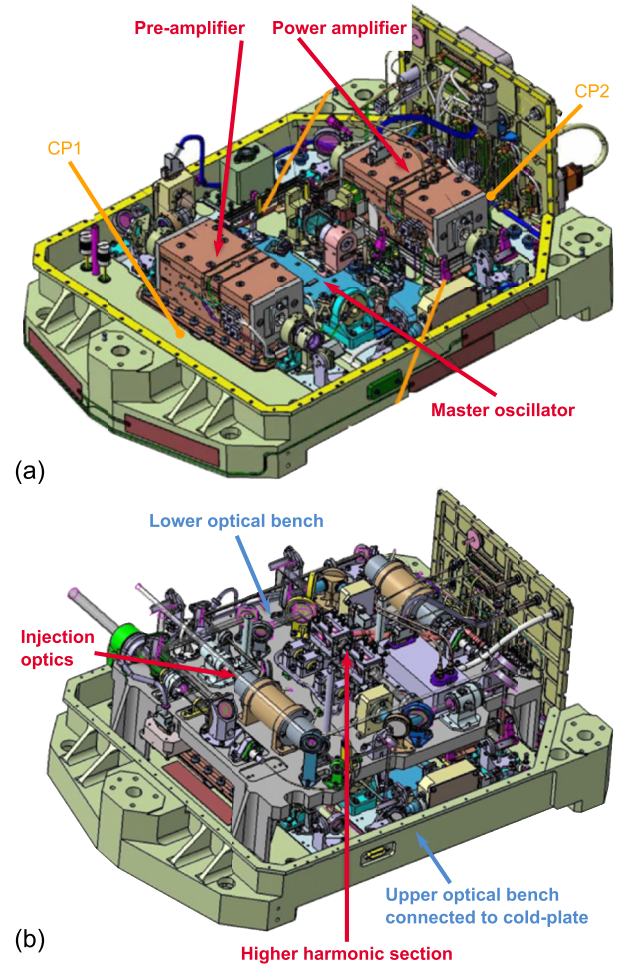

Fig. 2. Optical design of the ALADIN laser transmitter. (a) Upper optical bench, (b) lower optical bench, (c) photograph of the laser assembly.

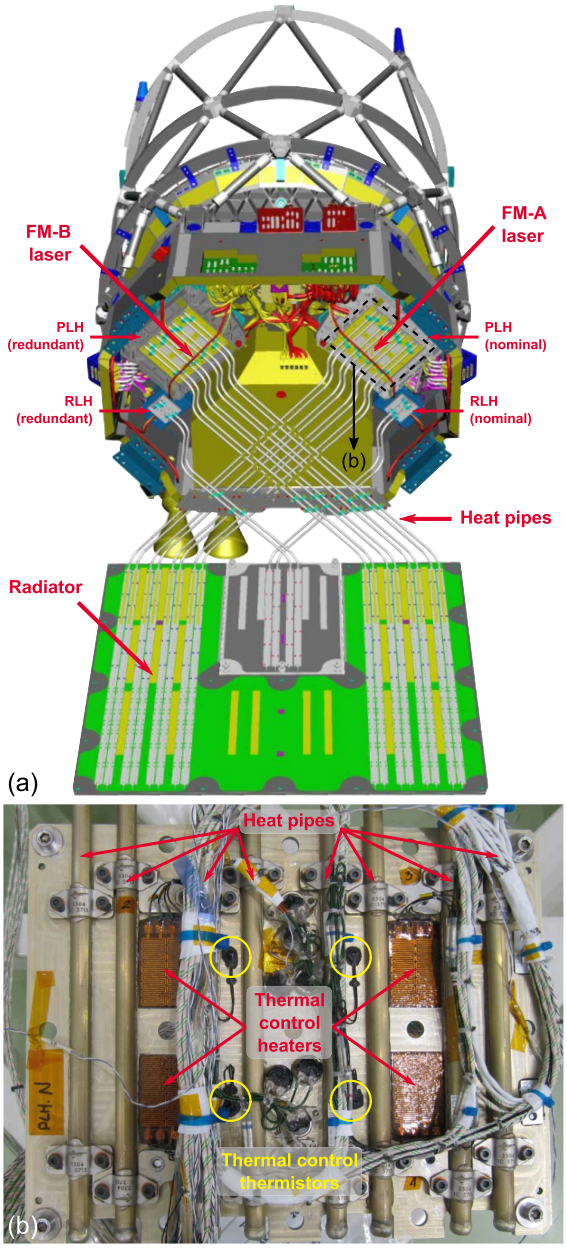

Fig. 3. ALADIN laser cooling system: (a) schematic showing the laser transmitters, heat pipes, and radiator (adapted from [1]). The upper optical bench of the laser is conductively cooled by the CP, which dissipates heat to a radiator via heat pipes. (b) Photograph of the CP for the nominal PLH (FM-A), highlighting the locations of the thermal control heaters and thermistors.

cold-plate (CP), with heat dissipated to a radiator on the side of the satellite via heat pipes. The design of this laser cooling system (LCS) and a photograph of the cold-plate are displayed in Fig. 3. The separation of active and passive elements required the MO to be positioned between the PreAMP and AMP, which had implications for the thermal sensitivity of the MO's alignment. Additionally, the arrangement across two optical benches necessitated a large number of beam-steering optics.

The PLH consisted of approximately 70 optical components, plus the monitoring detector assemblies including photodiodes. The upper optical bench served as the thermal interface with ALADIN, where the main heat loads were located. Total power dissipation ranged from 250 to 300 W, corresponding to a wall-plug efficiency of 1%–2%, given the average UV output power of 2 to 5 W during the nominal mission phase (40 to 100 mJ at 50.5 Hz pulse repetition rate; see Table 1).

The entire PLH unit weighed around 30 kg. Early in the pre-development phase, it was decided to operate the PLH in a vacuum to avoid the mechanical design issues associated with pressurization. Pressurization of a space laser involves managing structural integrity, thermal stability, and contamination risks. The laser housing must be strong enough to handle internal pressure and space vacuum while minimizing material fatigue and maintaining robust seals against leaks. Thermal expansion mismatches and trapped heat within the pressurized enclosure can misalign optics, so thermal management solutions are essential. Launch vibration and potential acoustic resonance can also affect the laser, requiring vibration-damping mounts and stable optical supports. Finally, preventing outgassing and radiation-induced material degradation is critical to ensure long-term reliability and maintain laser performance.

A. On-Ground Tests before Launch

The qualification and acceptance of the FM-A and FM-B lasers followed a standard process, including initial laser performance tests, a zero-gravity operability test, vibration simulations for launch, thermal vacuum testing, and a final performance assessment. Additionally, extended vacuum tests were conducted to study the long-term behavior over several weeks. Electromagnetic compatibility tests ensured proper function and minimal interference with the ALADIN instrument during flight [37].

The performance tests provided a comprehensive characterization of the laser system. For this purpose, a dedicated experimental setup, known as the optical ground support equipment (OGSE), was developed. The OGSE included holographic beam splitters to simultaneously measure key optical parameters, including energy, spatial, polarization, and temporal and frequency properties. These tests covered a broad range of frequencies and temperatures, allowing detailed cross-correlation of the data. Special focus was placed on monitoring critical parameters like pulse energy, frequency stability, divergence, and fluence, as they were essential for ensuring the overall performance of the ALADIN instrument.

The gravity test simulated weightlessness by positioning the laser heads in opposite directions relative to gravity and recording the aforementioned laser parameters. While heat dissipation was slightly affected by orientation and thus not fully representative of in-orbit conditions, the minor variation confirmed that the absence of gravity would not impact laser alignment. The vibration test subjected the RLH, PLH, and TLE to sinusoidal and random vibrations exceeding launch conditions. Performance tests before and after confirmed the integrity of the three units. The PLH, with its precisely aligned optical components, posed a particular challenge, but success was attributed to well-designed optical supports, rigorous testing during assembly, and careful laser alignment ensuring mechanical stability.

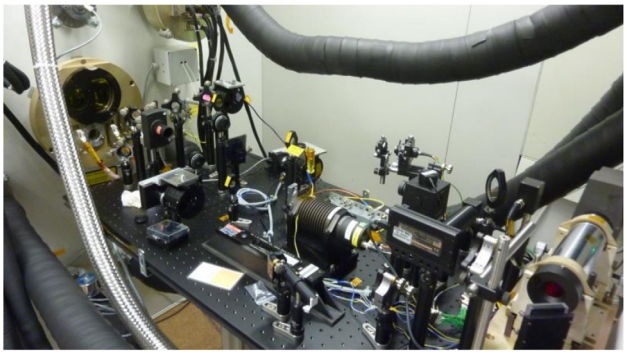

Fig. 4. Photograph of the OGSE in front of the vacuum chamber for assessing the laser performance under vacuum conditions. © (2024) SPIE. Reprinted, with permission, from A. Cosentino *et al.*, Proc. SPIE, **9626**, 96261U (2024) [37].

The thermal vacuum test was the most critical verification phase, as it evaluated the laser's stability in a vacuum and under significant temperature variations. These conditions impacted thermo-mechanical properties and optical performance, revealing many issues during early laser development. Key challenges included the stability of optical coatings, resonant cavity alignment, amplifier performance, and LIC. In particular, highly absorbing deposits due to LIC formed on the UV optics much faster than anticipated, despite stringent contamination control precautions, necessitating operation in a low-pressure oxygen environment, as explained in the next section. While solutions were found for each issue, they often required major realignments, leading to project delays. Figure 4 depicts the OGSE used during the test to simultaneously monitor the most important laser parameters.

To ensure the laser's robustness, three vacuum burn-in tests were performed—two on FM-A and one on FM-B—lasting four to six weeks each. The first test revealed significant damage to UV optical elements after a few weeks of continuous operation, leading to a change in the UV coating deposition technique. The second test identified two causes of energy reduction: rapid changes in thermal interface properties within the amplifiers and minor degradation of the laser diodes (−1%). The third test along with a final thermal vacuum test on the flight spare laser (FM-C) in 2015 demonstrated that stable laser operation could be achieved, with energy levels recoverable through adjustments to the laser settings. These results were further verified for both flight lasers during the thermal vacuum test of the full instrument, conducted at the Centre Spatial de Liège, Belgium, in late 2017. As a result of the on-ground verification campaign, both laser transmitters were confirmed to meet mission requirements and demonstrate long-term stability, validating the laser design.

B. Mitigation of Laser-Induced Contamination and Damage

In parallel to the laser on-ground verification, extensive test campaigns were conducted on all critical laser optics before their integration into the ALADIN instrument. These tests aimed to identify suitable high-power laser optics and reliable coating processes [38]. The extension of International Organization for Standardization (ISO) test standards for LID threshold testing—by incorporating larger test areas, long endurance tests, and an increased operational fluence safety margin—was crucial for ensuring the reliable operation of the ALADIN laser. Consequently, it was found that maintaining an ultra-clean environment was essential, achieved through constant purging of the laser emission path with pure molecular oxygen gas at pressure of up to 50 Pa. This oxygen environment was designed to prevent the accumulation of LIC which, together with LID, were identified as the most limiting factors for the lifetime of the UV laser, and thus the Aeolus mission [21,39].

Replenishment of the oxygen environment was facilitated by the in-situ cleaning system (ICS), which comprised two oxygen tanks, pressure regulators, and valves to control the pressures in the sealed cavities of the lasers and TRO, extending up to the telescope. Notably, there was a clear demarcation between the closed cavity of the PLH and the pressurized cavity of the sealed TRO, which were purged with oxygen at different pressure levels (PLH: <50 Pa, TRO: <190 Pa) and cycle durations (PLH: 4–5 h, TRO: 2–3 h). The oxygen supply was sufficient for the nearly five-year mission lifetime, which was ultimately constrained by the satellite's fuel, needed to maintain its orbit at 320 km—an altitude so low that it required weekly orbit correction maneuvers. Prior to activating the laser a few days after the launch of Aeolus in August 2018, the ICS primed the instrument sealed volumes twice to eliminate any residual contamination. Subsequently, the ICS was set to maintain operational oxygen pressure levels.

It should be noted that, in contrast to the ALADIN instrument on Aeolus, the laser transmitters used in ATLID on EarthCARE, although largely inherited from ALADIN, feature significant design differences. Most notably, the ATLID lasers do not utilize an ICS; instead, the laser housing is pressurized to 1.2 bar to prevent LIC and LID [40]. Additionally, electrical discharges caused by the operation of the high-voltage Q-switch in the MO at low pressures will be avoided. Since the output energy of the ATLID laser (35 mJ) is considerably lower than that of ALADIN, it uses only one amplifier module. Further differences between the ALADIN and ATLID designs are discussed in the outlook in Section 5.

3. LASER ENERGY

Monitoring of the laser status and performance was carried out based on telemetry (TM) data that was provided from several photodiodes (PDs) as well as numerous temperature and other sensors that were distributed in the different modules of the laser assembly. The TM parameters can be subdivided into observables, which were derived from measurements, and setting parameters, which were used for maintenance of the laser. Observables can be classified into energies, temperatures, cavity control parameters, electrical parameters (voltages, currents), and status flags. The locations of the most relevant PDs used for the assessment of the laser performance are indicated in Fig. 1. Pulse energies were measured after the exit of the MO (PD71), the PreAMP (PD72), the AMP (PD73), and the HHG section (PD74) by detecting the leakage through turning mirrors that guided the laser beam from one stage of the laser to the next. In addition, the energy of the residual green radiation

at 532 nm was detected on PD75 behind one of the dichroic mirrors that separated the UV beam from the other frequency components exiting the HHG section. The sampling rate of the TM parameters was 0.25 Hz.

Diffusion of the radiation incident on the photodiodes was achieved using a MACOR plate (machinable glass ceramic) oriented at a 45° angle to reflect the beam. The impact of speckle was determined to be negligible. The primary noise source in energy monitoring originated from the non-diffused, purely reflected portion of the beam from the MACOR plate, which exhibited a quasi-Gaussian profile and was sensitive to pointing variations. During the ALADIN instrument full performance (IFP) test, the UV energy measurement was calibrated. This calibration involved monitoring PD74 readings from each laser over a time span equivalent to one orbit, accounting for expected temperature fluctuations. Simultaneously, laser energy was measured using an energy meter positioned at the PLH output, behind a MACOR aperture stop. This stop reduced the beam diameter from 6.6 mm (86% encircled energy, EE) to 6.1 mm. The UV energy measurement met the specified accuracy requirement of $<2\%$ root mean square.

Converting PD74 readings to actual emitted energies at the PLH output required transfer curves and scaling factors to account for both the calibration of photodiode signals to the energy meter (measured before the aperture stop) and the optical loss introduced by the aperture stop. These scaling factors were determined to be 0.77 for the FM-A laser and 0.94 for the FM-B laser. A comparison of the correlation between PD74 readings and INT path signal levels, measured on the Mie channel detector during the IFP test, thermal vacuum test, and at the beginning of the mission, indicated good reliability for the FM-B scaling factor. However, significant long-term uncertainty (up to 10%) was observed for the FM-A scaling factor. Due to this uncertainty, the scaling factors are excluded from the subsequent discussions and plots of laser energy.

A. Energy Evolution and Influence of Cold-Plate Temperature

Shortly after the commencement of laser operation in space in September 2018, a decline in output energies of the first flight model laser (FM-A), particularly in UV emission, was detected by the internal PDs placed at various stages of the laser, as previously described. The temporal evolution of the UV energy measured with PD74 throughout the mission is depicted in Fig. 5. In addition to the initial UV energy being only 65 mJ, lower than the expected 80 mJ achieved on the ground, this parameter decreased by an average of 0.4 mJ per day during the first 14 days after power-on. Consequently, several adjustments to the laser parameters were carried out to alleviate the energy loss. In mid-September 2018, thermal adjustments were implemented in the two amplifiers, resulting in improved temperature distribution across the laser optical bench. Consequently, UV energy increased by 3 mJ, and the rate of decrease was significantly reduced to 0.14 mJ/day, or 1 mJ/week, aligning more closely with the performance observed on-ground for the FM-A laser.

Several temporary adjustments of the amplifier currents were performed to check the impact on the laser energy and fluence, and a permanent adjustment was made on December 15, 2018, elevating the UV energy by 12% to 57 mJ from which it dropped by the same rate of -1 mJ/week until the end of the four-month commission phase. A similar decrease rate was observed after the re-switch-on of FM-A following a failure detection isolation and recovery (FDIR) event that was caused by a global positioning system (GPS) reboot error in January 2019. It is interesting to note that the energy degradation trend continued during the one-month period when the laser was off (the amplifiers were operating during the majority of this non-lasing period). This suggested that the degradation was not due to the presence of the laser beam, i.e., not due to LID or LIC. The FM-A laser continued to be operated up until June 2019 when the energy had reached 40 mJ, and it was decided to switch to the second flight laser (FM-B), which, from on-ground tests, was known to be the better performing laser.

The switch between the two lasers was realized by the FFM, which enabled two stable configurations to direct either FM-A or FM-B onto the optical path of the ALADIN instrument. The FFM consisted of several mirrors and an optical invariant cube, all mounted on quasi-isostatic mounts. These components could be mechanically shifted by a binary paraffin actuator, which could be latched in either an extended or retracted position, corresponding to the two configurations needed to operate either FM-A or FM-B [41].

In accordance with the on-ground tests, the FM-B laser achieved a higher initial energy (67 mJ) compared to FM-A and exhibited a much slower decrease rate during the first months of operations. However, similar to FM-A, the output energy of FM-B varied by more than 10% during frequency scans. This frequency-dependent variation was sensitive to temperature changes of the CP on the laser bench that carried all active components of the laser, as mentioned earlier in the text. Although this observation provided a path to improve and stabilize laser performance, the root cause of the strong frequency dependence remained unresolved. Therefore, in March 2020, the CP temperatures were adjusted through thermal control heaters [see Fig. 3(b)] to ensure that the laser operated at its energy maximum during wind velocity mode, i.e., at the nominal laser frequency. This adjustment resulted in more stable energy output and reduced sensitivity to CP temperature fluctuations, and aligned the energy degradation rate with the expected slow ageing process of the pump laser diodes, showing a UV energy loss of about 25% over three years. This optimization of the laser's operating point in March 2020 is illustrated in the inset of Fig. 5 where the dashed red line indicates the gradual decrease of the energy maximum during the first year of FM-B. The purple curve depicts the UV energy modulation due to frequency scans during weekly instrument spectral registration (ISR) operations.

The set point change is also highlighted in Fig. 6, which tracks the temperatures measured by thermistors CP1 and CP2, both attached to the laser cold-plate at different locations on the upper optical bench inside the PLH [Fig. 2(a)]. As shown in Fig. 7, reducing the CP temperatures by ≈ 0.2 K caused a spectral shift of the frequency-dependent energy curve by about $+2.8$ GHz. This adjustment brought the spectral location of the energy maximum close to the nominal frequency at -3.75 GHz, which was the frequency set-point optimized for wind measurement with the spectrometers. Note that this

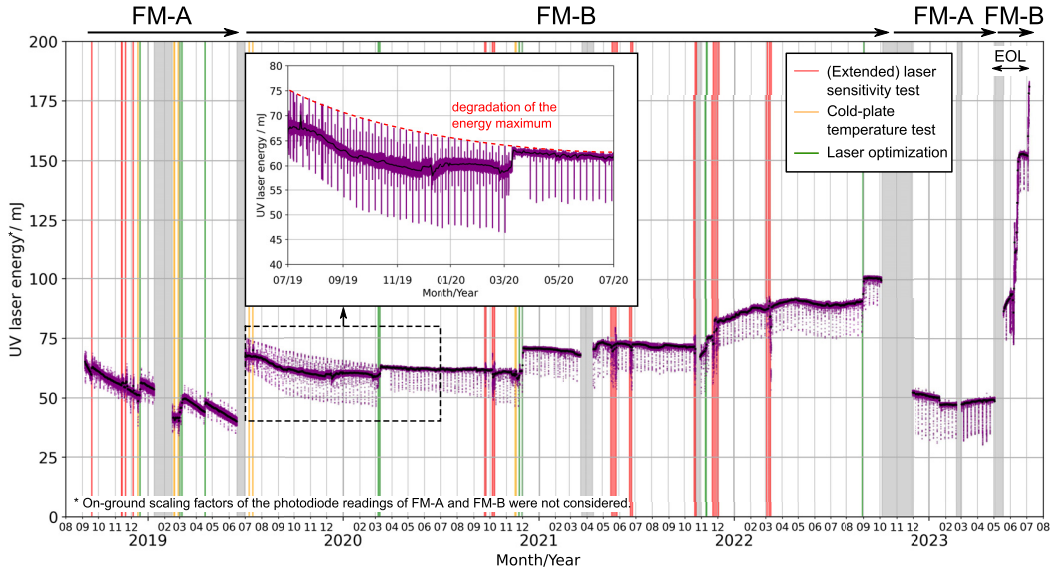

Fig. 5. Timeline of the UV output energy of the two ALADIN laser transmitters FM-A and FM-B over the mission period. The purple dots show the reading of the laser-internal photodiode with a temporal resolution of about 1 min, while the black dots represent the daily means. The pulse energy was increased up to 182 mJ during the last days of operations in July 2023 in the frame of the end-of-life (EOL) activities. The frequency dependence of the laser energy results in an energy modulation during the weekly calibrations (see inset and text). Periods when the laser was temporarily switched off are indicated by gray-shaded areas. The vertical bars mark periods of laser activities: red, (extended) laser sensitivity test; yellow, CP temperature test; green, laser optimizations with permanent setting changes. Laser tests that were carried out in the frame of the EOL phase are not illustrated.

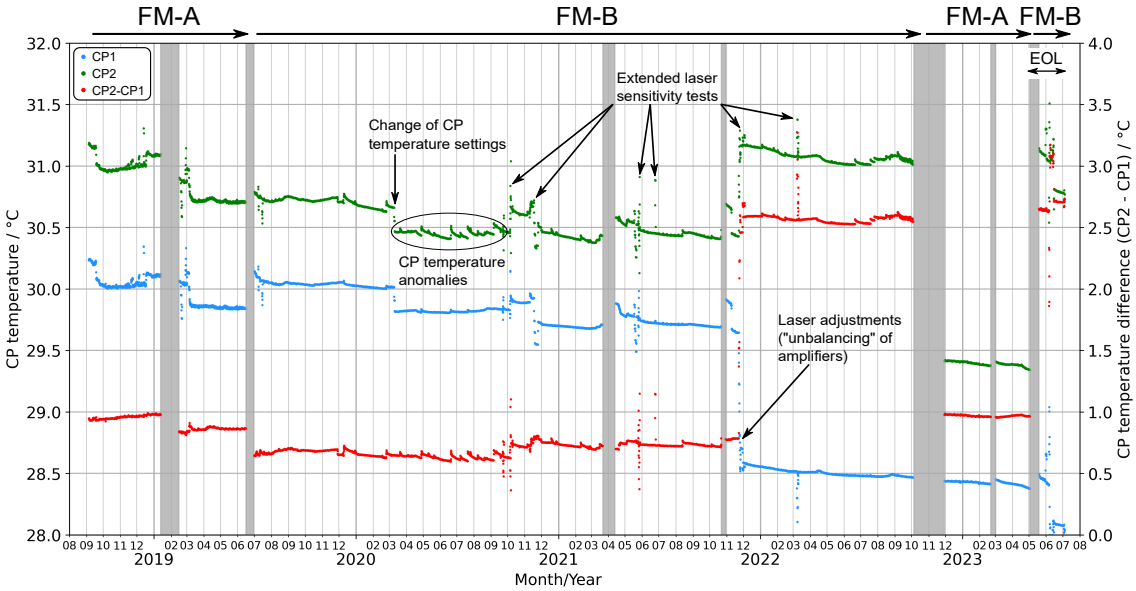

Fig. 6. Timeline of the cold-plate temperatures CP1 (blue) and CP2 (green) of the two ALADIN laser transmitters FM-A and FM-B over the mission period (left ordinate). The temperature difference CP2 minus CP1 is plotted in red (right ordinate). Periods when the laser was temporarily switched off are indicated by gray-shaded areas.

frequency is relative, given in the UV domain, with values defined such that 0 GHz is at the center of the mode-hop-free scanning range of the RLH—approximately 4 GHz in the IR and 12 GHz in the UV. The absolute frequency is determined by the ultra-low-expansion cavity to which the RLH is locked. The improved stability was consistent across all laser energies (MO, PreAMP, AMP), demonstrating that the laser operated at a more stable working point after the CP temperature adjustment in March 2020. Although the root cause of the frequency dependence remains undetermined, a parasitic etalon effect within the MO is a likely candidate, potentially explaining the observed high temperature sensitivity of about −14 GHz/K in the UV and −4.7 GHz/K in the IR, correspondingly.

The critical relationship between the CP temperature and the frequency dependence of the laser energies was further explored in a dedicated CP sensitivity test conducted in May 2021.

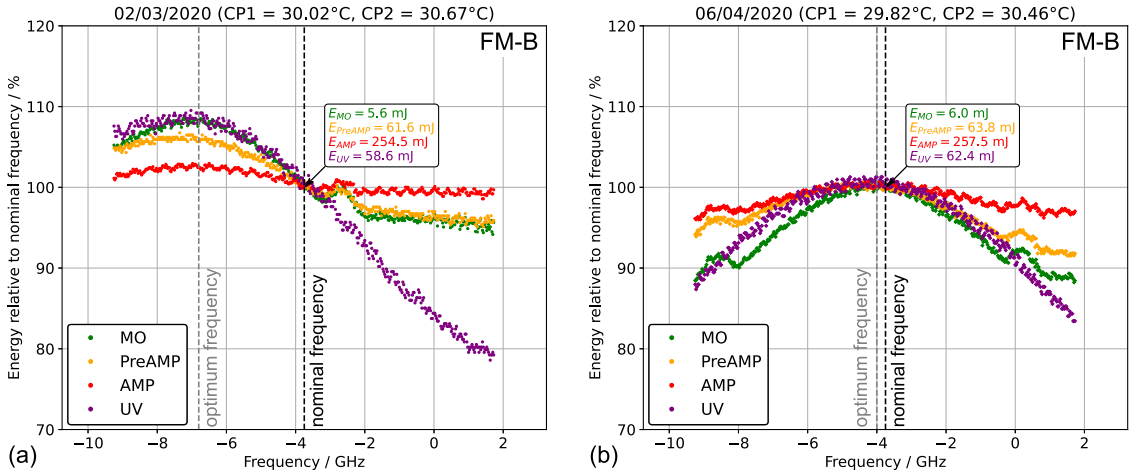

Fig. 7. Frequency dependence of the FM-B laser energies measured at the output of the MO (green), the PreAMP (orange), the AMP (red), and the UV conversion stage (purple) derived from the Instrument Spectral Registration (ISR) on (a) March 2, 2020, and (b) April 6, 2020, at different CP temperatures. The nominal frequency at −3.75 GHz is indicated by a vertical dashed line while the optimum frequency where the energies are highest is marked by a gray vertical line.

During this test, the temperature was adjusted over a range of 0.4 K, from 29.47°C to 29.87°C, in 0.1 K increments. At each temperature setting, the frequency was scanned across a range of 11 GHz with a resolution of 25 MHz, similar to the procedure used during ISRs to characterize the transmission curves of the Fizeau interferometer and the Fabry–Pérot interferometers in the Mie and Rayleigh channels of the ALADIN receiver, respectively [34]. The resulting curves of the different laser energies (MO, PreAMP, AMP, and UV) as a function of frequency are displayed in the left panels of Fig. 8. For each curve, the optimum frequency—where the energy reaches its maximum—was determined and plotted against the CP temperature in the corresponding right panel. Linear fits were applied to each of these plots to derive the temperature sensitivity k of the optimum frequency for the four laser energies.

The plots in Fig. 8 show that the optimum frequency shifts to shorter wavelengths as CP temperature increases. The temperature sensitivities range from $k_{\mathrm{AMP}} = -10.3$ GHz/K for the power amplifier to $k_{\mathrm{MO}} = -13.6$ GHz/K for the master oscillator. These variations in sensitivities are due to the uncertainty in determining the optimum frequency, which spans a relatively broad spectral range, particularly for the AMP and UV energies. Additionally, beyond the spectrally broad primary energy maximum, secondary maxima are observed in the MO and PreAMP energies, although they are absent in the UV energy. The frequency scan of the AMP energy also revealed a narrowband modulation with a period of approximately 400 MHz, corresponding to about 133 MHz in the IR domain. These observations indicate a complex interplay of frequency-dependent losses inside the MO cavity, saturation effects in the two amplifier stages, and the nonlinear conversion process in the HHG section. Additionally, it is possible that the energy measurements at the PDs, which detected leakage radiation through highly reflective (HR) mirrors, were slightly influenced by the frequency of the incident light via interference effects at the coatings. The results from the CP temperature sensitivity test were confirmed with a similar increase in the atmospheric lidar return and thus were crucial for the subsequent operation of both lasers. These optimization activities significantly shaped the strategies for improving and stabilizing laser performance in the following years of the mission.

B. Laser Activities

Thanks to the optimization of the CP temperature in March 2020, stable laser operation of the FM-B was achieved over 40 months until October 4, 2023, only interrupted by two additional FDIR events in March and October 2021. Both FDIRs were triggered by a failed consistency check by the on-board software on the operational mode of the instrument during calibration and monitoring procedures that involved a frequency scan of the laser. Although the frequency commands were correctly uplinked to the satellite, the frequency settings were corrupted on instrument level in these two incidents ultimately causing ALADIN to be switched down to survival mode. It is worth noting that the time for the recovery of the instrument including the ramp-up of FM-B took not more than 10 days in March and even less than six days in October in comparison to the re-switch-on of the FM-A laser in January 2019, which took about one month. The FDIR in March involved a change in the emitted frequency of the reference laser head, which necessitated an adaptation of the nominal frequency and the Rayleigh spectrometer temperature in order to optimize the spectral working point of the instrument.

During FM-B operation, a significant signal decrease was observed along the emission path between the laser output and the telescope, with a nearly constant decline rate of −1% per week. This finding was confirmed by ground-based measurements of the laser energy at the Pierre Auger Observatory, a facility primarily designed for detecting ultra-high-energy cosmic rays. The energy was derived through the reconstruction of the laser beam's path from space to the ground [42]. To counteract the signal loss, the laser energy was incrementally increased to over 100 mJ, mainly by raising the diode pump currents of

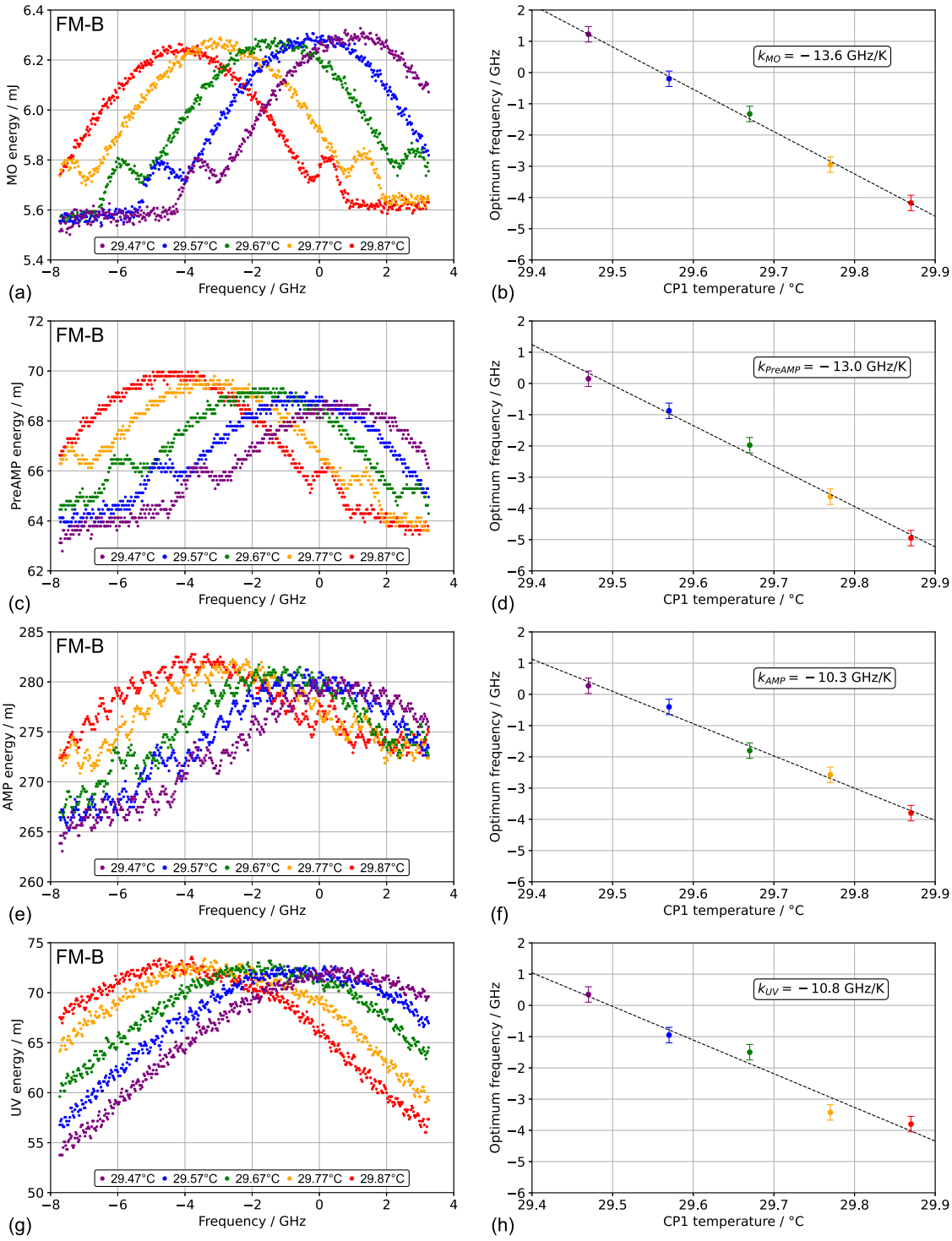

Fig. 8. Relationship between CP temperature (CP1) and optimum frequency of the FM-B laser. The left panels depict the frequency-dependent energies measured at the output of the (a) MO, (c) the PreAMP, (e) the AMP, and (g) the UV conversion stage, derived from ISRs at five different CP temperatures. The right panels [(b), (d), (f), (h)] show the corresponding temperature dependence of the optimum frequency where the respective energy is highest together with a linear fit. The slope of the fit is given in the inset. The error bars indicate the uncertainty in the optimum frequency derived from the curves in the left panels.

the MO, and/or by reducing the delay between the MO pulse emission and the amplifier pumping phase.

Furthermore, the alignment of the FM-B laser beam along the instrument path, which was worse compared to the FM-A laser, was optimized through multiple laser adjustments. These adjustments involved altering the heating currents of the PreAMP and AMP in opposite directions ("unbalancing"), which helped to steer the laser beam along the horizontal axis to

some extent. However, this procedure had an impact on the CP temperatures, particularly because the MO arrangement was positioned between the two amplifier blocks on the laser bench (see Fig. 2). Consequently, subsequent tuning of the CP temperatures was necessary to maintain the maximum laser energy at the spectral position of the nominal frequency, as illustrated in Fig. 7(b).

This fine-tuning was notably achieved in late November 2021, when CP1 was reduced by 1.0 K and CP2 was increased by 0.8 K, thereby adjusting the temperature gradient (CP2–CP1) from 0.8 K to 2.6 K. As shown in Fig. 6, this temperature change was significant compared to typical CP temperature anomalies, which were usually less than 0.1 K. Despite their small magnitude, these anomalies affected the laser energies by a few percent. Most of these anomalies were triggered by orbit correction maneuvers, where the satellite thrusters were operated. However, their frequency decreased after an adjustment of the top floor heaters outside the laser assembly in May 2021. This adjustment notably reduced seasonal temperature variations, particularly during the eclipse season, and platform maneuvers.

Over the 40 months of FM-B operation, the laser performance remained well within specifications and was consistent with the on-ground test results. The laser energy degradation was primarily due to the expected ageing of the laser components, especially the degradation of the laser pump diodes in the MO and amplifiers. The black dots in Fig. 9 depict the temporal evolution of the IR energy that was measured with PD73 at the output of the AMP before the beam enters the HHG section (Fig. 1). The IR energy was increased step-wise several times, mainly by reducing the delay between the emission of the MO pulse and the amplifier pump phase: from 75 µs to 60 µs in November 2020, and to 50 µs in December 2021. Additionally, the MO pump power was increased from the initial 61 A to 63 A in November 2021, and to 67 A in late August 2022.

A minor enhancement in IR energy was also achieved by unbalancing the amplifiers, when the heating currents of the PreAMP and AMP were decreased and increased by 1.6 A, respectively. This procedure aimed primarily at optimizing the beam alignment to improve transmission along the instrument optical path, necessitating an adaptation of the CP temperatures, as previously mentioned.

The optimization of the CP temperature set point in March 2020 is also visible in Fig. 9, which additionally shows the assumed IR laser energy if laser optimizations had not been performed and the CP temperatures had been optimized from the beginning of FM-B operation. The blue data points between switch-on of FM-B in June 2019 and the CP temperature tuning in March 2020 represent the maximum energies measured during the frequency scans of the weekly ISR modes, similar to the UV energy spikes in the inset of Fig. 5. By calculating the relative gain in IR energy for each optimization activity and dividing by the respective value, the hypothetical IR energy without these measures is approximated. The resulting blue curve demonstrates that the energy evolution followed an exponential decline with a loss of about 20% over more than three years of FM-B operation, which is consistent with estimations based on on-ground tests and pump diode ageing effects (see Section 3.F).

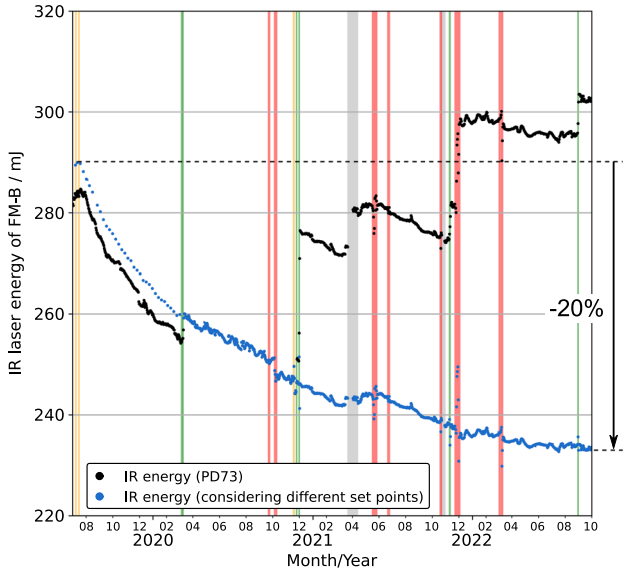

Fig. 9. Timeline of the IR energy of the FM-B laser over its 40-month operation. The black dots represent the energy at the output of the power amplifier, measured with photodiode PD73. The blue dots describe the assumed energy if laser optimizations had not been performed and the laser had been operated at the optimum CP temperature set point already before March 2020. The vertical bars mark periods of laser activities, using the same color-coding as in Fig. 5.

The stable operation of the FM-B laser is also attributed to the absence of LIC inside the laser housing. Despite the slow energy degradation, the voltage applied to the thermoelectric cooler to maintain the temperatures of the HHG crystals remained stable during the FM-B phase. This stability suggests that the thermal load on the crystals was constant, indicating that there were no external factors, such as increased absorption from LIC deposits, necessitating adjustments in voltage to compensate for temperature changes. Moreover, LIC would have led to uneven heating, causing temperature fluctuations that would have disrupted phase matching, thereby reducing the HHG conversion efficiency. In contrast, the conversion efficiency from IR to UV actually increased from about 23% in July 2019 to more than 30% in 2022. This improvement was mainly due to the greater fluence inside the HHG crystals, resulting from increased IR energy and a smaller beam diameter, particularly after the MO pump power was increased.

Despite the excellent performance of the FM-B laser, the drastic signal loss along the instrument emission path inside the sealed TRO of more than 70% by mid-2022 prompted the decision to switch back to the FM-A laser in October/November 2022. The assumption that the signal loss was confined to the optics unique to the FM-B laser output beam was confirmed by the complete recovery of transmission between the laser and telescope following the switch back to the FM-A laser. Specifically, the loss was confined to the input window of the TRO and the relay optics within, including two HR turning mirrors and an optical invariant cube of the FFM, which directed the redundant FM-B laser beam onto the nominal optical path. The exact mechanism of this loss is still under

investigation, with LIC and LID or darkening due to the activation of color centers in this limited number of optics currently considered the most likely causes.

Additionally, a small portion (<10%) of the total loss recorded by the ALADIN detectors can be attributed to clipping of the atmospheric backscatter signal at the instrument field stop, due to the poorer alignment of the FM-B output beam along the instrument path compared to FM-A. The clipping loss was quantified through image analysis by comparing the far-field beam distribution of the atmospheric return signal, regularly measured with the Rayleigh channel detector in imaging mode after propagation through the field stop, to simulated signal distributions with and without clipping. Additional insights were provided by the Pierre Auger Observatory, which quantified signal loss along the emission path, as detailed in [42]. During the FM-B period, the measured laser energy degradation at the telescope output was slightly smaller than the signal decrease observed on the receiver channels. This 5%–10% discrepancy aligns with the findings from the image analysis.

Leveraging the insights gained during the FM-B period, particularly regarding the interplay between CP temperatures, frequency, and laser energy, the FM-A laser was optimized according to the procedures developed in previous years. The frequency dependence of the FM-A laser energies at the initial CP temperature set point in 2018 and after the optimization in the second FM-A period in 2023 is shown in Fig. 10.

Reducing CP1 and CP2 by approximately 1.7 K resulted in a stable performance of the FM-A laser at an energy of around 50 mJ over five months until the end of the operational mission on April 30, 2023. During the second FM-A period, another FDIR was triggered on February 21, 2023, when a spurious energy spike was detected on the MO PD, thereby exceeding a set energy threshold and ultimately causing the instrument to go into survival mode. The recovery took one week.

C. Monitoring of the Laser Beam Profile

The laser beam profile was monitored in orbit on a weekly basis using a dedicated laser beam monitoring (LBM) mode. This method involved analyzing the INT path signal, i.e., the small fraction of the laser output directly guided to the instrument's receiver via a free optical path (see Section 2), using the Mie spectrometer. By scanning the laser frequency across the Fizeau interferometer's free spectral range, Mie interference fringes were recorded at various adjacent positions on the 16×16 image zone of the detector. During the LBM, the detector operated in the so-called imaging mode, in contrast to the lidar mode used for range-resolved wind observations [36]. This procedure enabled the reconstruction of the illumination profile incident on the Fizeau interferometer, which was used to approximate the near-field laser beam profile, assuming ideal INT path transmission.

The LBM images revealed a stable Gaussian intensity distribution of the FM-A laser beam, whereas the FM-B laser showed a more elliptical shape, as depicted in Fig. 11. However, due to increasing transmission loss along the optical path behind the laser output during the FM-B phase, the LBM images no longer accurately represented the FM-B beam profile. Instead, they illustrated the degradation of the relay optics in the front optics, as mentioned above. After reverting to the FM-A laser in autumn 2022 by retracting the relay optics, optical path transmission was restored, and the LBM images recorded through the mission's end closely matched those from the initial FM-A phase, indicating stable beam profile characteristics.

Despite their low optical resolution, the LBM images were essential for assessing the laser's fluence levels and, therefore, were a crucial element of laser activities. Additionally, they provided valuable insight into the spectrometers' illumination profiles of the INT path, aiding in overall instrument performance assessment. It is recommended to implement similar beam monitoring capabilities in future lidar missions where fluence and illumination characteristics are relevant.

Measurement of the beam quality factor, M^2, in the x- and y-directions was not feasible in orbit. However, the close match between the LBM images obtained in orbit and those from

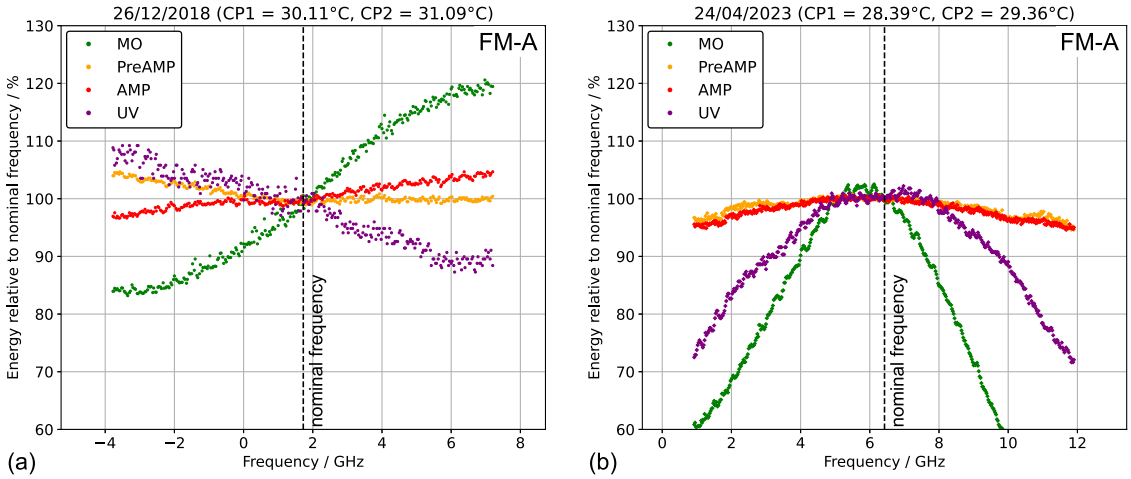

Fig. 10. Frequency dependence of the FM-A laser energies measured at the output of the MO (green), the PreAMP (orange), the AMP (red), and the UV conversion stage (purple) derived from the Instrument Spectral Registration (ISR) on (a) December 26, 2018, and (b) April 24, 2023, at different CP temperatures. The respective nominal frequency is indicated by a vertical dashed line.

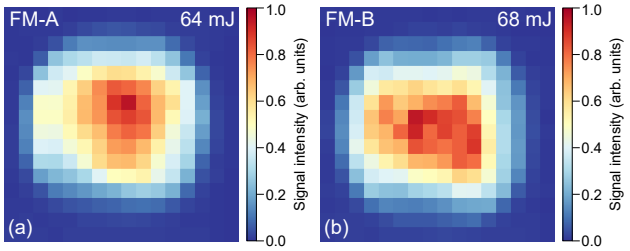

Fig. 11. Laser beam profiles of the (a) FM-A and (b) FM-B lasers, obtained from laser beam monitoring (LBM) measurements conducted on September 4, 2018, and July 1, 2019, respectively. The average energy, measured using the PD74 sensor, is indicated in the top right of each LBM image.

pre-flight ground tests suggests that the beam quality remained consistent with on-ground characterizations, where M^2 values were better than 3.5 in both directions [23], satisfying laser requirements.

D. End-of-Life Activities

Following the conclusion of nominal operations for ALADIN, a series of special tests, referred to as EOL activities, was conducted to address various instrument-related and scientific questions. These tests also allowed the lasers to operate near maximum output energy, a condition avoided during the operational phase due to the higher fluence on the optics and the associated risk of LID. After a final switchover to the more powerful FM-B laser in mid-May 2023, its output energy was successively increased by boosting the MO and amplifier pump currents, by reducing the amplifier phasings and *Q*-switch duration, as well as by optimizing the heating currents while adapting the CP temperatures, as described above. Starting from the set point applied until October 2022, the energy was first raised to 111 mJ on June 9 and then to 151 mJ on June 15, 2023, where it remained stable in the following three weeks (see Fig. 5). The MO pump currents were then increased by 2 A, from 67 A to 69 A. Additionally, the PreAMP and AMP pump currents were scaled up by 2 A to 70.5 A and 68 A, respectively, enhancing the UV energy output up to 180 mJ. During its final 33 h of operation on July 4 and July 5, 2023, the ALADIN FM-B laser transmitter delivered even up to 182 mJ of output energy without any sign of degradation inside the laser. This set a new record for a UV laser operated in space after one of the two LITE lasers had reached 169 mJ over about 21 h already in 1994 [13]. The high output power was also achieved thanks to an enhanced IR-to-UV conversion efficiency of nearly 50%, which resulted from a reduced beam size and consequently increased intensity within the HHG crystals. Based on the laser near-field beam parameters, as provided in Table 1, the average power density of the two ALADIN lasers ranged from approximately 15 Wcm^{-2} during the late FM-A phase to 70 Wcm^{-2} at the final EOL setting.

An overview of the most relevant laser activities and switch-on procedures performed during the Aeolus mission including the EOL phase is provided in Table 2. The laser activities can be classified into extended sensitivity tests (13, indicated by red vertical bars in Fig. 5), CP temperature tests (seven, yellow) and laser optimizations with permanent changes (12, green). The frequency of laser tests varied significantly throughout the mission. During the first half year, many tests were conducted to optimize and stabilize the FM-A laser, particularly its thermal conditions. In contrast, fewer tests were performed during the early FM-B phase. As the signal loss in the emission path increased, several tests were carried out to improve the laser beam alignment along the instrument path. Additionally, the laser energy was increased multiple times to counteract the degrading transmission through the optics behind the laser output.

E. Interruptions of the Laser Operation

Between the first switch-on of FM-A in early September 2018 and the final switchdown of FM-B on July 5, 2023, laser operation was temporarily suspended seven times for various reasons. An overview of all interruptions, both commanded and related to FDIRs, is provided in Table 3. The four FDIRs between January 2019 and February 2022, as well as the two laser switches in June 2019 and October 2022, were already mentioned earlier in the text. Another FDIR event occurred during the EOL phase on May 3, 2023, caused by a commanding issue related to threshold settings in preparation for an upcoming test. Multiple attempts to switch the FM-A laser back on were unsuccessful. Detailed analyses of the housekeeping telemetry data ultimately pointed to a hardware failure in the TLE, which prevented the power supply to the power amplifier module. As a result, the switchover to the FM-B laser, initially planned for later in the EOL phase, was rescheduled to mid-May.

As a lesson learned for future space lidar missions, the FDIR system should be made more efficient by distinguishing whether an alarm is real or just caused by a transient event, such as the MO energy spike in the FM-A in February 2023. Additionally, the necessity of switching down the entire instrument to standby mode or if a switch to intermediate modes is sufficient in case of an FDIR should be evaluated.

F. On-Ground Tests with the FM-C Laser

In addition to the two flight model lasers used in the ALADIN instrument, a third laser, the FM-C, was built by Leonardo S.p.A. to perform extended on-ground laser tests under mission-like conditions in a vacuum. FM-C also served as a spare in case any critical issues arose with FM-A or FM-B before launch. The FM-C laser tests were pivotal in preparing for and extending the operational life of the Aeolus mission. From February to August 2016, the life time test (LTT) conducted on FM-C simulated the vacuum conditions that the ALADIN lasers would encounter in space, providing a long-term assessment of their performance. The LTT enabled a comprehensive evaluation of the laser's stability and degradation, particularly its UV energy output, which decreased by only about 5% over the six-month test period. This degradation rate was lower than that identified in the FM-A and FM-B lasers, and was attributed to the longer test duration, which allowed for more accurate estimates of the laser's performance, especially given the nonlinear degradation curve observed later in space (Fig. 9). The decline in laser energy was primarily due to the ageing of the pump laser diodes. Other potential causes, such as LIC and LID, were ruled out after 745

Table 2. List of Laser Activities during the Aeolus Mission and the Resulting UV Output Energy

Date	Activity	UV Energy after Activity
03/09/2018	Start of operations with FM-A	50.8 mJ
04/09/2018	Finalization of FM-A laser settings	64.5 mJ
18/09/2018	Laser optimization	59.8 mJ ↗ 63.6 mJ
13/11/2018	Laser sensitivity test	55.4 mJ
20/11/2018	Laser sensitivity test	54.5 mJ
04 to 05/12/2018	Laser sensitivity test	52.4 mJ
17 to 18/12/2018	Laser optimization	51.1 mJ ↗ 56.8 mJ
14/01/2019	Stop of operations (GPS error)	
15/02/2019	Continuation of operations with FM-A	42.1 mJ
18 to 20/02/2019	CP temperature sensitivity test	41.3 mJ
26 to 27/02/2019	CP temperature sensitivity test	41.5 mJ
01/03/2019	Laser optimization	41.4 mJ ↗ 46.0 mJ
05 to 06/03/2019	Laser optimization	46.0 mJ ↗ 49.8 mJ
17/04/2019	Laser optimization	44.1 mJ ↗ 48.3 mJ
16/06/2019	Stop of operations, switchover to FM-B	
28/06/2019	Start of operations with FM-B	66.2 mJ
08/07/2019	CP temperature sensitivity test	67.6 mJ
15/07/2019	CP temperature sensitivity test	67.5 mJ
06/03/2020	Laser optimization	59.0 mJ ↗ 59.8 mJ
09 to 10/03/2020	Laser optimization	59.8 mJ ↗ 63.2 mJ
21 to 24/09/2020	Extended laser sensitivity test	61.5 mJ
05 to 10/10/2020	Extended laser sensitivity test	60.0 mJ
17 to 19/11/2020	CP temperature sensitivity test	58.1 mJ
24/11/2020	Laser optimization	59.2 mJ ↗ 60.9 mJ
30/11 to 01/12/2020	Laser optimization	61.1 mJ ↗ 70.6 mJ
22/03/2021	Stop of operations (wrong mode error)	
01/04/2021	Continuation of operations with FM-B	72.8 mJ
17 to 27/05/2021	CP temperature sensitivity test	72.7 mJ
21 to 25/06/2021	Extended laser sensitivity test	72.3 mJ
19 to 22/10/2021	MO sensitivity test	—
22/10/2021	Stop of operations (wrong mode error)	
28/10/2021	Continuation of operations with FM-B	66.8 mJ
09 to 11/11/2021	Laser optimization	69.8 mJ ↗ 75.0 mJ
22/11 to 03/12/2021	Extended laser sensitivity test and laser optimization	75.8 mJ ↗ 82.1 mJ
07 to 11/03/2022	Extended laser sensitivity test	87.9 mJ
30 to 31/08/2022	Laser optimization	90.2 mJ ↗ 100.7 mJ
04/10/2022	Stop of operations, switchover to FM-A	
28/11/2022	Start of operations with FM-A	52.2 mJ
21/02/2023	Stop of operations (MO energy spike)	
28/02/2023	Continuation of operations with FM-A	47.4 mJ
30/04/2023	Stop of nominal operations	
01/05/2023	Start of EOL activities with FM-A	49.5 mJ
03/05/2023	Stop of operations (erroneous commanding, TLE failure)	
17/05/2023	Continuation of EOL activities with FM-B	84.5 mJ
06 to 09/06/2023	Extended laser sensitivity test and laser optimization (EOL)	93.2 mJ ↗ 110.5 mJ
12 to 15/06/2023	Extended laser sensitivity test and laser optimization (EOL)	111.2 mJ ↗ 150.8 mJ
03 to 05/07/2023	Laser optimization (EOL)	151.5 mJ ↗ 180.2 mJ
05/07/2023	Final shutdown of FM-B	

million laser shots at full energy, as the near-field laser beam profiles showed no significant changes from the beginning to the end of the test. Additionally, the LTT revealed subtle issues, such as an unexpected mechanical drift in the MO along the horizontal axis, which was not immediately apparent in shorter tests. Although this drift did not significantly affect the UV energy during the test, its discovery underscored the importance of long-duration testing, as such issues might only become visible after extended operation. The LTT not only validated the laser design but also offered an opportunity to develop recovery strategies and prepare in-orbit procedures to manage any anomalies that could occur during the mission.

Following the mission's launch, the FM-C laser was delivered to the ESA European Space Research and Technology Centre (ESTEC) in Noordwijk, The Netherlands. Here, a dedicated test facility, the Laser Operation Verification Facility (LOVF),

Table 3. Interruptions of the Laser Operation during the Mission[a]

Date and Time of Laser Switch-Off	Commanded or FDIR	Reason for Interruption	Date and Time of Continuation at Nominal Laser Settings
14/01/2019, 01:41 UTC	FDIR (system level)	GPS error	15/02/2019, 20:10 UTC
16/06/2019, 19:00 UTC	Commanded	Switchover to FM-B	28/06/2019, 15:22 UTC
22/03/2021, 02:57 UTC	FDIR (instrument level)	Failed consistency check by the on-board software; wrong mode error	01/04/2021, 10:41 UTC
22/10/2021, 14:18 UTC	FDIR (instrument level)	Failed consistency check by the on-board software; wrong mode error	28/10/2021, 10:36 UTC
04/10/2022, 14:34 UTC	Commanded	Switchover to FM-A	28/11/2022, 22:33 UTC
21/02/2023, 03:27 UTC	FDIR (laser level)	Energy spike in master oscillator	28/02/2023, 08:55 UTC
03/05/2023, 13:20 UTC	FDIR (instrument level)	Erroneous threshold commands during preparation of EOL activity; re-switch-on failed due to malfunction of the FM-A transmitter laser electronics; switchover to FM-B	17/05/2023, 16:00 UTC
05/07/2023, 14:30 UTC	Commanded	Final switch-down before re-entry	—

[a]See Supplement 1 for explanation of the acronyms.

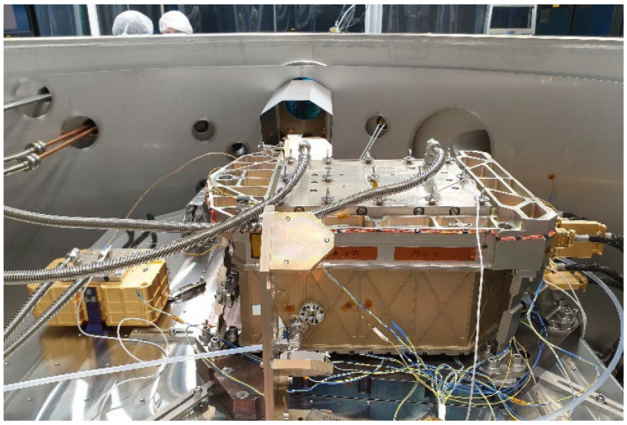

Fig. 12. Photograph of the LOVF with the RLH (left) and the PLH (right) of the FM-C laser inside the vacuum chamber.

was established. The LOVF housed a vacuum chamber for the PLH and RLH, an ICS to supply oxygen to the PLH, and an OGSE to measure the key laser parameters (Fig. 12). The LOVF vacuum chamber was a cylinder with a height of 1.2 m and a diameter of 1.5 m. This facility was essential for fine-tuning the laser's operational parameters before applying them in flight, ensuring a low-risk approach to laser adjustments during the mission. For example, tests at the LOVF helped resolve issues like micro-vibrations affecting frequency stability and allowed engineers to safely test critical parameter changes by validating them on the ground first. This included pushing the laser's operational limits, such as increasing the MO energy beyond the 5 mJ threshold, previously thought to risk damaging the cavity mirrors. The success of these tests at the LOVF demonstrated that the laser could safely exceed this limit, enabling an increase in the MO pump currents to 67 A in August 2022, which boosted the MO energy to 7.4 mJ. This, in turn, raised the UV energy to over 100 mJ, enhancing the Aeolus mission's data quality.

The FM-C laser tests were critical in verifying the laser's behavior, identifying and mitigating potential issues, and increasing confidence in handling the laser during the mission. These findings proved invaluable, particularly in extending the mission life and improving its overall performance.

4. FREQUENCY STABILITY

The frequency stability of the ALADIN lasers was assessed based on the analysis of the INT path signal from the Mie channel, which was available on single-pulse level. As the outgoing laser frequency is represented by the centroid position of the interference fringe that is produced by the Fizeau spectrometer and imaged onto the Mie detector, the temporal variations of this fringe position, also referred to as Mie response, can be interpreted as laser frequency fluctuations. Previous studies have shown that the influence of alignment variations on the Mie response is negligible [26]. However, it was found that the amplitude of the response variations depends on the location of the Mie fringe on the detector due to the nonlinearity of the Mie response with respect to frequency. This is important when comparing the results for the FM-A and FM-B lasers, as the instrument was operated at different nominal fringe positions on the detector during the mission. Conversion of the Mie response into relative laser frequency is based on response calibration data from which a sensitivity of approximately 100 MHz per pixel was determined as an average across the entire detector and mission period. The accuracy of the relative laser frequency determination is estimated to be 1 MHz and is mainly limited by the shot-noise-limited signal-to-noise ratio of the Mie signal and the FWHM of the interference fringe (≈ 2.0 px ≈ 200 MHz).

The frequency stability was calculated as the standard deviation, σ_f, over 540 pulses emitted during a 12 s wind observation. This averaging length corresponds to a horizontal resolution of 86 km, meeting the user requirement. The total number of pulses is determined by the number of pulses, P, for which atmospheric return signals are accumulated on board the spacecraft into so-called "measurements," and the number of measurements, N, that are combined into one observation during post-processing. For most of the Aeolus mission, P was set to 19 and N to 30. In December 2021 and April 2022, the P/N

settings were adjusted to 38/15 and later to 114/5 to increase signal levels at the measurement scale relative to the readout noise [36]. Since the signal from one pulse was always lost during the ALADIN detector readout, the total number of laser pulses for the default P/N setting was $(19-1)\cdot 30 = 540$. Although this number increased to 555 and later 565 in subsequent mission phases, only the first 540 pulses from each observation were considered in the frequency stability analysis for consistency and comparability.

A. Influence of the Satellite's Reaction Wheels

The assessment of the frequency stability revealed pulse-to-pulse fluctuations σ_f of less than 12 MHz (mean over one orbit repeat cycle of one week) throughout the mission and even less than 9 MHz when considering the nonlinearity of the Mie response. The excellent frequency stability was achieved despite the repeated occurrence of short periods with significantly enhanced frequency noise, reaching up to $\sigma_f = 100$ MHz, which were found to coincide with specific rotation speeds of the satellite's reaction wheels. This result suggested that the root cause was micro-vibrations that deteriorated the laser stability on timescales of a few tens of seconds. The existence of these "critical" reaction wheel speeds entailed a clustering of observations with enhanced frequency variations in specific regions of the Earth, forming linear and circular structures around the globe [26]. The identified detrimental frequencies of the reaction wheels ranged between 14 and 28 rotations per second (RPS) and were consistent among the three active wheels, although the relative impact on the two lasers was different.

Analysis of the Aeolus wind error with respect to ECMWF model winds showed that the temporally degraded frequency stability of the ALADIN laser transmitter had only a minor impact on the wind data precision on a global scale, which was 3 to 4 ms^{-1} for the Mie winds and 5 to 9 ms^{-1} for the Rayleigh winds, respectively [7]. The small overall impact is primarily due to the limited percentage of wind measurements where frequency fluctuations were significantly elevated. Although the Mie wind systematic error increased by 0.3 ms^{-1} during periods when frequency stability exceeded 20 MHz, the small contribution (4%) of these cases rendered this effect negligible (<0.1 ms^{-1}) when considering all wind data. The impact on the systematic and random error of the Rayleigh winds was insignificant even at high frequency noise compared to the Poisson noise and readout noise affecting the Rayleigh spectrometer response. This dominance of other noise sources is primarily attributed to the atmospheric return signal level being lower than expected by a factor of 2.5 to 3, the root cause of which is still under investigation [43]. Similar results were demonstrated for the apparent speed of the ground returns that were measured with the Mie and Rayleigh channels of the ALADIN receiver. Here, the application of a frequency stability threshold that filters out wind observations with variations larger than $\sigma_f = 20$ MHz improves the accuracy of the Mie and Rayleigh ground velocities by only 0.1 ms^{-1} at the expense of useful ground data [26].

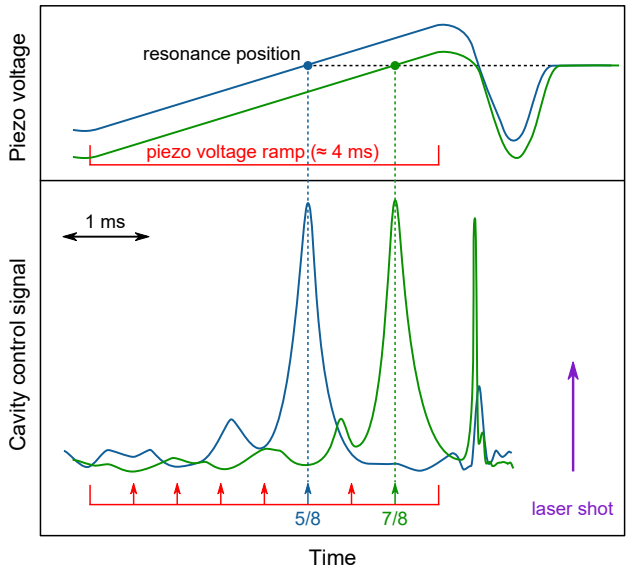

Fig. 13. Cavity control sequence of the ALADIN laser master oscillator, showing the final 6 ms of the 20 ms period between two successive laser pulses as measured during on-ground tests. Depending on the offset applied to the piezo mirror voltage (top graphs), the cavity control signal (bottom graphs) exhibits resonance at either 5/8 (blue lines) or 7/8 (green lines) of the total duration of the piezo voltage ramp.

B. Improvement of the Cavity Length Stabilization

One of the EOL activities aimed to improve the laser frequency stability by adjusting the laser cavity length control loop (CLCL) parameter, which defined the locking of the seed laser with the MO cavity resonance. The CLCL scanned the MO cavity length by using a piezo actuator to move the output coupling mirror. This process aligned the cavity resonance with the RLH seed radiation and established the correct cavity length for the laser shot to ensure single-longitudinal-mode operation. The CLCL algorithm, based on the ramp-hold-fire technique, introduced a variable offset voltage to the scanning voltage ramp to track the resonance peak evolution over time and keep it at a specified point, e.g., in the center, of the voltage ramp [31].

The top graphs in Fig. 13 show the temporal evolution of the voltage applied to the piezo mirror, including the scanning ramp with a duration of approximately 4 ms. The remaining part of the sequence serves to mitigate voltage hysteresis of the piezo actuator. The bottom graphs represent the CLCL signal used for the detection of the cavity resonance. Depending on the voltage offset, the resonance is registered at different times during the ramp. For most of the mission lifetime, the CLCL ramp parameter was set to 5/8 of the ramp duration (blue lines). During the EOL test, the set point was changed to 7/8 (green lines), reducing the delay between detection of the resonance and laser pulse emission by about 1 ms. The 5/8 setting was chosen as the default based on on-ground experience during the development phase, when the detrimental impact of the reaction wheels was not present.

The test was performed for both lasers on April 19 (FM-A) and May 29, 2023 (FM-B), and improved the frequency stability in both cases by a factor of two, reaching values of 4 to 6 MHz (see Table 4). Moreover, the portion of observations with large frequency fluctuations ($\sigma_f > 15$ MHz) was considerably

Table 4. Laser Frequency Stability of the Two ALADIN Lasers and Percentage of Wind Observations with Degraded Stability for One-Week Periods before and after the CLCL Ramp Set Point Changes on April 19, 2023 (FM-A), and May 29, 2023 (FM-B), Respectively

Laser	FM-A	FM-A	FM-B	FM-B
Parameter	CLCL ramp set point 5/8	CLCL ramp set point 7/8	CLCL ramp set point 5/8	CLCL ramp set point 7/8
Frequency stability (σ_f over 540 pulses)	8.2 MHz	4.5 MHz	11.6 MHz	6.3 MHz
Percentage of observations with $\sigma_f > 10$ MHz	24.9%	5.6%	45.1%	5.6%
Percentage of observations with $\sigma_f > 15$ MHz	9.1%	1.0%	20.3%	0.9%
Percentage of observations with $\sigma_f > 25$ MHz	1.2%	<0.1%	4.3%	<0.1%

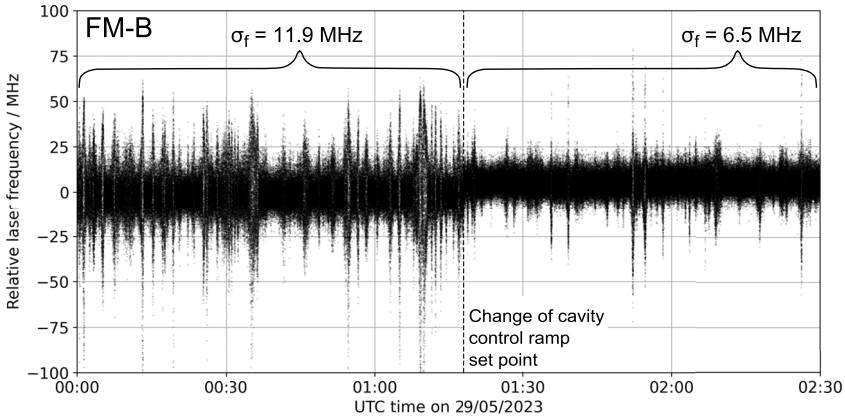

Fig. 14. Time series of the FM-B laser frequency fluctuations over 2.5 h on May 29, 2023, including the cavity control set point change at 1:18 UTC, indicated by the vertical dashed line. The given values denote the standard deviation σ_f over 540 pulses, as defined in the text.

reduced from 9% (FM-A) and 20% (FM-B) to only 1%, indicating that the lasers were less susceptible to micro-vibrations caused by the reaction wheels at their critical rotational speeds due to the shortening of the time delay between resonance detection and pulse emission.

The impact of the CLCL set point change is visible in Fig. 14, which depicts the time series of the FM-B laser frequency at the pulse-to-pulse level over a period of 2.5 h on May 29, 2023, when the position of the cavity resonance was shifted from 5/8 to 7/8 of the ramp duration at 1:18 UTC. Before the setting change, the frequency fluctuated by 11.9 MHz with periods when the frequency stability was strongly degraded due to micro-vibrations caused by the reaction wheels. Note that of the three reaction wheels operated during the mission, wheels #1 and #2 had the strongest influence, whereas both lasers were almost insensitive to the rotations of wheel #3 [26]. After the set point change, the frequency fluctuations were significantly reduced to 6.5 MHz, as the perturbations from the reaction wheels were less detrimental.

A similar result was achieved with the FM-A laser when the ramp voltage was adjusted such that the resonance peak was detected about 1 ms later in the CLCL sequence, as described above. Here, the frequency stability was $\sigma_f = 8.2$ MHz at the 5/8 CLCL ramp setting and improved to $\sigma_f = 4.5$ MHz at the 7/8 CLCL ramp setting. A long-term time series of the FM-A laser frequency stability over 13 days, surrounding the point in time when the set point was changed on April 19, 2023, is shown in Fig. 15(a). The black line represents the hourly mean of σ_f, while the gray-shaded area describes the variability of this value in terms of the scaled median absolute deviation (MAD) [26]. In addition to the improvement in average frequency stability, the variability of this parameter has decreased at the new set point, indicating smaller amplitudes of the frequency noise at times when the reaction wheels rotate at their critical speeds.

This observation is supported by the plots depicted in Figs. 15(b) and 15(c), which illustrate the frequency stability σ_f in dependence on the rotational speed of the two reaction wheels #1 (x-axis) and #2 (y-axis). Each dot represents one wind observation period of 12 s within the nearly one-week periods of both CLCL settings plotted in Fig. 15(a). The point pattern reflects the correlation between two of the three reaction wheels used to control the satellite's attitude over one repeat cycle of a week. The cross-hatch pattern created by the color-coding of the data points visualizes the critical speeds of both wheels, with wheel #2 showing approximately 10 critical speeds between 16 and 26 RPS. The perturbation of wheel #1 was strongest at around 22.4 RPS and 26.2 RPS, leading to enhanced frequency fluctuations at the 5/8 set point. In contrast, after optimizing the CLCL setting, the FM-A laser was no longer susceptible to the micro-vibrations introduced by wheel #1. The influence of wheel #2 was also largely mitigated, as evidenced by the less pronounced horizontal stripes in Fig. 15(c) compared to Fig. 15(b). The percentage of wind observations with $\sigma_f > 15$ MHz was reduced from $\approx 9\%$ to 1%, while fluctuations $\sigma_f > 25$ MHz no longer occurred at all. The same is true for the FM-B laser.

For both lasers the frequency stability was improved by approximately 45%, although the absolute values differ significantly (see Table 4). As mentioned earlier in the text, this

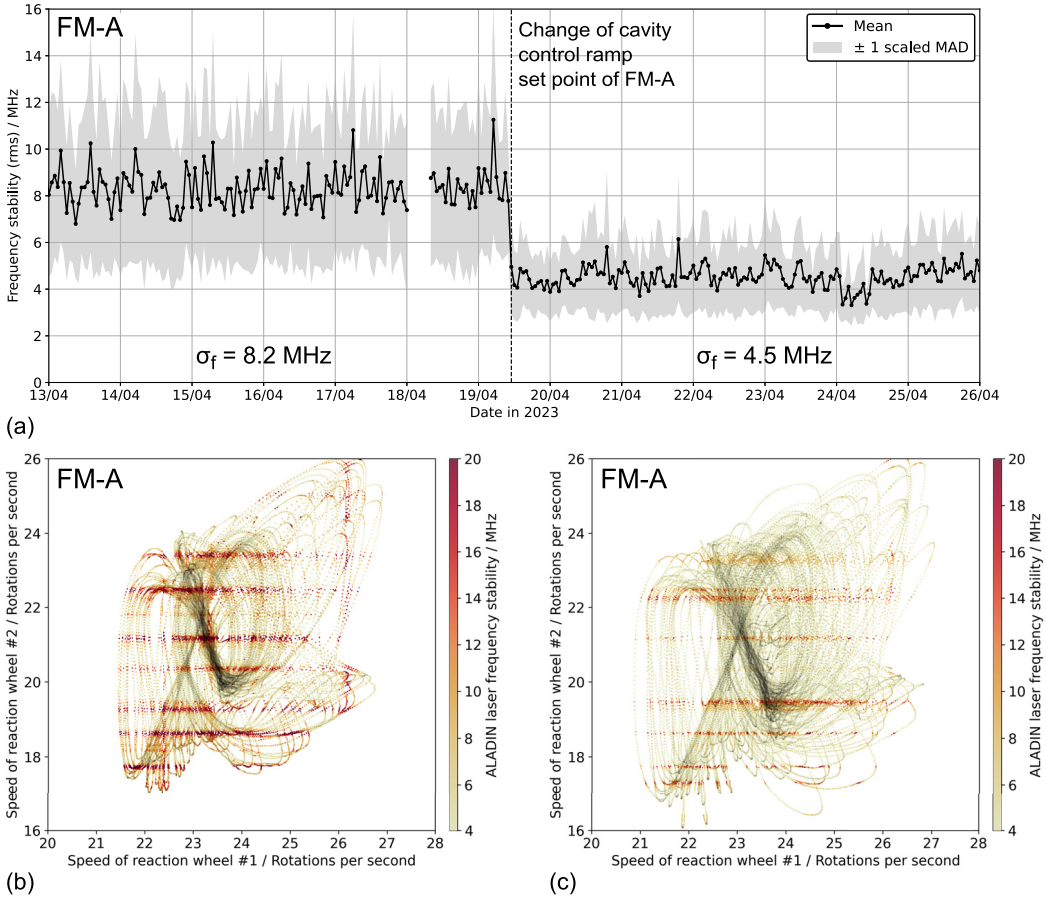

Fig. 15. Laser frequency stability of the FM-A: (a) hourly mean of the frequency fluctuations (black line) and the scaled median absolute deviation (scaled MAD, gray shaded area) between April 16 and 23, 2023, including the cavity control set point change on April 19, 2023, at 11 UTC, indicated by the vertical dashed line. The bottom panels show the frequency stability in dependence on the rotational speeds of the satellite's reaction wheels 1 and 2 for the nearly one-week periods (b) before and (c) after the set point change.

discrepancy arises from the nonlinearity of the Mie response with respect to frequency. Specifically, the so-called pixelation effect involved a modulation of the measured Mie fringe centroid position as the fringe moves across the detector. As a result, frequency fluctuations of a certain magnitude cause different response variations depending on the fringe's position on the detector. During the EOL tests with the FM-B laser, the fringe was located near the center of the detector, close to a local maximum of response sensitivity. In contrast, when testing with the FM-A laser, the Mie fringe was positioned in the right half of the detector, where changes in the fringe centroid position were less affected by the pixelation effect. Consequently, the measured frequency variations for the FM-A laser were smaller than those for the FM-B laser, despite the performance of both transmitters being expected to be similar, as suggested by on-ground assessments using an external wavemeter [24]. Accurate correction for the pixelation effect is challenging due to the temporally varying intensity distribution incident on the Mie spectrometer throughout the Aeolus mission. This variation gradually altered the pixelation pattern and, consequently, the Mie response sensitivity over longer time scales [44].

Given the considerable improvement in laser frequency stability, the 7/8 CLCL ramp setting was maintained following the FM-B test on May 29 for the remainder of the Aeolus mission until the final shutdown of the instrument on July 5, 2023. In conclusion, the outcome of the EOL activity was a significant success, demonstrating the capability of both lasers to produce highly frequency-stable UV emission even after nearly five years in orbit and despite the presence of micro-vibrations.

5. SUMMARY AND OUTLOOK

The successful operation of the UV laser transmitters onboard the Aeolus satellite marked a significant milestone in spaceborne lidar technology. During the operational phase of the world's first Doppler wind lidar mission, from September 2018 to April 2023, the two switchable lasers generated more than 7 billion nanosecond laser pulses in the UV spectral region, with energies ranging from 40 to 100 mJ. The first laser, FM-A, experienced a rapid decline in output energy due to a gradual misalignment of the master oscillator, which was caused by thermal drift of the laser bench. This thermal drift resulted in a non-optimal temperature set point of the master oscillator depending on the emitted laser frequency. Upon switching to the second laser, FM-B, energy degradation was limited to the expected slow ageing process of the pump laser diodes, leading to an energy loss of about 20% over 40 months of FM-B operation from June 2019 to October 2022.

Owing to a drastic decrease of more than 70% in atmospheric return signal levels during this period, the laser energy was increased incrementally to over 100 mJ to compensate for the signal loss, which was caused by degradation of the optics responsible for guiding the FM-B laser beam onto the instrument's nominal optical path toward the telescope. Additionally, the performance of the FM-B laser was optimized by regulating its thermal environment, which affected laser energy depending on the emission frequency, most likely due to a parasitic etalon effect in the master oscillator. The knowledge gained about the relationship between CP temperatures, frequency, and energy was then applied to the FM-A laser after switching back in November 2022, ensuring stable output energy around 50 mJ and restored transmission along the emission path toward the telescope.

During the final weeks before the instrument's ultimate shutdown, comprehensive laser activities were conducted to explore the potential for further optimizing laser performance using methods that were considered too risky during the mission's operational phase. These tests were highly successful, demonstrating the capability to operate the laser at energies well beyond 100 mJ over several weeks. Furthermore, the frequency stability was significantly improved by adjusting the cavity control sequence of the master oscillator, thereby reducing the time between detecting the seed laser resonance and pulse emission. This adjustment mitigated the impact of micro-vibrations that had previously deteriorated laser frequency stability at specific rotation speeds of the satellite's reaction wheels. As a result, frequency fluctuations were reduced by a factor of two for both lasers to less than 7 MHz (standard deviation over the period of one wind observation of 12 s). Given this remarkable outcome, it is recommended to conduct dedicated tests across the full range of commandable parameters prior to the launch of Earth Explorer missions. This approach would enable the safe exploration of these parameters during instrument tests in the commissioning phase, potentially leading to significant performance enhancements.

Aeolus provided groundbreaking wind data on a global scale, improving numerical weather prediction and enhancing our understanding of atmospheric dynamics. This success was not without formidable challenges, particularly laser-induced contamination and damage, which has historically hindered the long-term operation of UV lasers in space. Overcoming these challenges required the development and implementation of advanced technologies. A pivotal innovation was the introduction of the ICS, which provided the optics in the laser and emission path of the instrument with low pressures of oxygen (50–100 Pa). This effectively mitigated the accumulation of contaminants on the laser optics and ensured that the laser maintained its high output power for the duration of the entire mission. In addition to the ICS, improved optics coatings were another crucial advancement, significantly reducing the rate of LID. However, the ICS did not function as expected for the TRO, where LIC is one of the most likely root causes of the signal loss experienced during the FM-B period. In addition to the HR turning mirrors and the optical invariant cube of the FFM, the window separating the laser housing from the TRO setup is a candidate for this issue. Positioned far from the oxygen inlet at the end of a long, narrow bellow tube, it likely received insufficient oxygen to prevent LIC.

The technological breakthroughs were essential in addressing the issues that had plagued previous space lidar missions and now serve as a benchmark for future missions employing UV lasers. The insights and data gained from Aeolus have provided a strong foundation for subsequent missions like EarthCARE [19], launched in May 2024, and Aeolus-2 [45,46], scheduled for launch in the mid-2030s. These missions are based on a similar laser technology operating at the same UV wavelength. However, unlike ALADIN, the transmitters on EarthCARE and Aeolus-2 will employ pressurized lasers to further enhance the reliability and longevity of the laser systems by maintaining a stable operational environment, thereby reducing the risks associated with contamination and damage.

Building on the success of the Aeolus Earth Explorer mission, the operational Aeolus-2 mission will be conducted in cooperation with the EUMETSAT Polar System (EPS) Programme and is therefore also referred to as EPS-Aeolus. The mission will involve two satellites launched in succession, ensuring at least 10 years of operation. Its primary objective is to provide Europe and the international community with the unique capability to measure atmospheric winds for the support of NWP and to improve the understanding of atmospheric dynamics and associated processes. While ESA will be responsible for developing and manufacturing the two satellites and their instruments, EUMETSAT will be responsible for the development and provision of the ground segment, procuring the launch services, and operating the satellites for at least 10 years. This includes processing the acquired data and delivering it to users [47–49]. The partnership between ESA and EUMETSAT in developing Aeolus-2 will follow the proven collaboration model used in the Meteosat Third Generation and MetOp Second Generation Programmes.

By the end of 2024, the Aeolus-2 mission entered phase B2, which involves the verification of the preliminary design against project and system requirements, culminating in the Preliminary Design Review. In terms of the laser transmitter, apart from the adoption of a pressurized assembly, the design should retain as much of the ALADIN laser technology as possible to minimize development risks. During phase B1, two separate laser transmitter prototypes (or engineering models) were developed in parallel. The first transmitter was built at Leonardo S.p.A. based on the heritage from ALADIN and ATLID currently being operated onboard EarthCARE. The second engineering model was developed at the Fraunhofer Institute for Laser Technology (ILT) building on the Future Laser (FULAS) technology [50], which is also incorporated into the laser transmitter of the Methane Remote Sensing Lidar Mission (MERLIN) [51], scheduled for launch in 2029. Both concepts have met the stringent requirement to deliver more than 150 mJ of UV output power, a significant increase from the 80 mJ required for Aeolus, which was assessed to be feasible with current laser technologies. The energy scaling was motivated by the requirement for higher vertical resolution in wind profiles to further enhance the positive impact of the wind observation on NWP forecasts [46]. Consequently, higher laser power is necessary to achieve a sufficiently high signal-to-noise ratio and reduce the wind random error for higher vertical or horizontal

resolution, especially for Rayleigh wind measurements, which are predominantly affected by Poisson noise [52].

Another consideration is wall-plug efficiency, which is generally low for diode-pumped solid-state lasers, particularly after frequency conversion. In the ALADIN transmitters, efficiency was further reduced because the lasers were initially designed and optimized for higher energy emissions, specifically between 110 and 120 mJ. After the development phase, however, the laser's energy output was intentionally reduced to mitigate LID on the instrument optics. This change in the operating set point was not re-optimized for amplification efficiency, resulting in a further reduction in wall-plug efficiency to approximately 1%–2% for the operational laser, compared to 2%–3% in the originally optimized configuration (based on UV beam power relative to power-electronics consumption). For Aeolus-2, a more efficient design is anticipated with a fully optimized operating set point, likely achieving wall-plug efficiency within the upper range of 2%–3% noted above.

The significant signal loss on the emission path outside the laser transmitter during the FM-B phase—most likely caused by long-term LIC and LID, and/or the darkening of optics due to the activation of color centers—was a key factor in the decision to transition from a monostatic (transceiver) design to a bi-static configuration [53]. This modification separates the high-fluence emission path from the reception path, thereby enhancing the instrument's robustness and reducing the number of optics susceptible to LIC and LID. However, the bi-static configuration necessitates the use of a co-alignment system to actively stabilize the overlap between the transmitter and receiver. To achieve this, a co-alignment sensor is integrated into the receiver path to monitor the beam pointing and divergence of the atmospheric return signal, which is then corrected by a beam steering mechanism within the transmitter. This technique is inherited from ATLID, which also employs a bi-static design [40].

Similar to the development phase of the Aeolus mission, the implementation of an airborne demonstrator has been recommended by the Aeolus-2 Science Advisory Group as part of a risk-reduction strategy. Thanks to its high technological commonality with the ALADIN instrument onboard Aeolus, the A2D [54–56] has proven invaluable for gaining a deep understanding of the instrument's calibration procedures, operations, and performance based on real atmospheric measurements. A next-generation airborne demonstrator would offer operational testing capabilities, complimentary to those currently envisaged for the on-ground testing of the Aeolus-2 instrument, during both mission preparation and execution, fully leveraging the new design features—particularly the co-alignment sensor, which has already been operated and optimized for the A2D for many years [57]. Additionally, in parallel with the development of the Aeolus-2 mission, the A2D laser transmitter is planned to be upgraded to a new model manufactured by the Fraunhofer ILT, delivering 60 mJ of UV output energy at a higher pulse repetition frequency of 100 Hz.

In conclusion, the stable and dependable operation of the ALADIN laser transmitters on the Aeolus satellite represents a major advancement in space-borne lidar technology. The mission not only improved global weather predictions and advanced our understanding of atmospheric dynamics, but also provided valuable lessons in overcoming the challenges associated with UV-laser-induced contamination and damage. These insights, combined with technological innovations will shape future missions like EarthCARE and Aeolus-2. In partnership with EUMETSAT, the Aeolus-2 mission is set to build on Aeolus's legacy with improved design features, ensuring a more robust and long-lasting performance. These advancements will enable more precise wind measurements, further improving weather forecasting and deepening our understanding of atmospheric processes for years to come.

Funding. European Space Agency (40000126336/18/I-BG, 4000144330/24/I-AG).

Acknowledgment. The authors acknowledge the Aeolus Mission Advisory Group, the Aeolus Space and Ground Segment Operations teams, the European Laser Risk Reduction Working Group, and the Technical Directorate of the European Space Research and Technology Centre for their invaluable contributions in the development of the ALADIN lasers. The authors are also especially grateful to all partners involved in the planning, execution and analysis of the Aeolus end-of-life activities: the Aeolus Flight Operation Segment (FOS), the Aeolus Mission Management and Planning Facility (MMPF), the Aeolus Payload Data Ground Segment (PDGS), Leonardo S.p.A., Airbus Italia, Airbus Defence and Space (Toulouse), Airbus Defence and Space (Stevanage), the European Space Research and Technology Centre (ESTEC) and the Aeolus Data Innovation and Science Cluster (DISC). Their collaboration and commitment were vital to the successful completion of the tests.

Disclosures. The authors declare no conflicts of interest.

Data availability. Data underlying the results presented in this paper are not publicly available at this time but may be obtained from the authors upon reasonable request.

Supplemental document. See Supplement 1 for supporting content.

REFERENCES

1. E. Andersson and P. Clissold, eds., "ADM-Aeolus science report," ESA SP-1311 (ESA Communications Production Office, 2008).
2. O. Reitebuch, "The spaceborne wind lidar mission ADM-Aeolus," in *Atmospheric Physics: Background–Methods–Trends*, U. Schumann, ed. (Springer, 2012), pp. 815–827.
3. A. Martin, M. Weissmann, and A. Cress, "Investigation of links between dynamical scenarios and particularly high impact of Aeolus on numerical weather prediction (NWP) forecasts," Weather Clim. Dyn. **4**, 249–264 (2023).
4. V. Pourret, M. Šavli, J.-F. Mahfouf, *et al.*, "Operational assimilation of Aeolus winds in the Météo-France global NWP model ARPEGE," Q. J. R. Meteorol. Soc. **148**, 2652–2671 (2022).
5. G. Halloran and M. Forsythe, "Assessment for operational assimilation of horizontal line of sight winds from the European Space Agency's Aeolus at the Met Office," Q. J. R. Meteorol. Soc. **150**, 2869–2887 (2024).
6. M. P. Rennie, L. Isaksen, F. Weiler, *et al.*, "The impact of Aeolus wind retrievals on ECMWF global weather forecasts," Q. J. R. Meteorol. Soc. **147**, 3555–3586 (2021).
7. M. Rennie and L. Isaksen, "The NWP impact of Aeolus Level-2B winds at ECMWF," ESA Contract Report, Aeolus DISC Contract No. 4000126336/18/I-BG (European Centre for Medium-Range Weather Forecasts, 2024).
8. M. Ern, M. A. Diallo, D. Khordakova, *et al.*, "The quasi-biennial oscillation (QBO) and global-scale tropical waves in Aeolus wind observations, radiosonde data, and reanalyses," Atmos. Chem. Phys. **23**, 9549–9583 (2023).
9. C. J. Wright, R. J. Hall, T. P. Banyard, *et al.*, "Dynamical and surface impacts of the January 2021 sudden stratospheric warming in novel Aeolus wind observations, MLS and ERA5," Weather Clim. Dyn. **2**, 1283–1301 (2021).

10. K. Sun, G. Dai, S. Wu, *et al.*, "Effect of wind speed on marine aerosol optical properties over remote oceans with use of spaceborne lidar observations," Atmos. Chem. Phys. **24**, 4389–4409 (2024).
11. T. Flament, D. Trapon, A. Lacour, *et al.*, "Aeolus L2A aerosol optical properties product: standard correct algorithm and Mie correct algorithm," Atmos. Meas. Tech. **14**, 7851–7871 (2021).
12. P. Wang, D. P. Donovan, G.-J. van Zadelhoff, *et al.*, "Evaluation of Aeolus feature mask and particle extinction coefficient profile products using CALIPSO data," Atmos. Meas. Tech. **17**, 5935–5955 (2024).
13. D. M. Winker, R. H. Couch, and M. P. McCormick, "An overview of LITE: NASA's lidar in-space technology experiment," Proc. IEEE **84**, 164–180 (1996).
14. J. B. Abshire, X. Sun, H. Riris, *et al.*, "Geoscience Laser Altimeter System (GLAS) on the ICESat mission: on-orbit measurement performance," Geophys. Res. Lett. **32**, 405 (2005).
15. A. J. Martino, J. Cavanaugh, A. Gibbons, *et al.*, "ICESat-2/ATLAS at 4 years: instrument performance and projected life," Proc. SPIE **12512**, 125120A (2023).
16. D. Winker, M. Vaughan, and B. Hunt, "The CALIPSO mission and initial results from CALIOP," Proc. SPIE **6409**, 640902 (2006).
17. M. J. McGill, J. E. Yorks, V. S. Scott, *et al.*, "The Cloud-Aerosol Transport System (CATS): a technology demonstration on the International Space Station," Proc. SPIE **9612**, 96120A (2015).
18. G. Dai, S. Wu, W. Long, *et al.*, "Aerosol and cloud data processing and optical property retrieval algorithms for the spaceborne ACDL/DQ-1," Atmos. Meas. Tech. **17**, 1879–1890 (2024).
19. A. J. Illingworth, H. W. Barker, A. Beljaars, *et al.*, "The EarthCARE satellite: the next step forward in global measurements of clouds, aerosols, precipitation, and radiation," Bull. Am. Meteorol. Soc. **96**, 1311–1332 (2015).
20. J. E. Yorks, M. J. McGill, S. P. Palm, *et al.*, "An overview of the CATS level 1 processing algorithms and data products," Geophys. Res. Lett. **43**, 4632–4639 (2016).
21. L. Mondin, F. F. Era, H. Kheyrandish, *et al.*, "Caveats and pitfalls of high energy UV laser operation on ground," Proc. SPIE **10562**, 105621U (2017).
22. A. Cosentino, A. D'Ottavi, A. Sapia, *et al.*, "Spaceborne lasers development for ALADIN and ATLID instruments," in *IEEE International Geoscience and Remote Sensing Symposium* (2012), pp. 5673–5676.
23. A. Cosentino, A. Mondello, A. Sapia, *et al.*, "High energy, single frequency, tunable laser source operating in burst mode for space based lidar applications," Proc. SPIE **10568**, 1056817 (2017).
24. L. Mondin and P. Bravetti, "Aeolus high energy UV laser wavelength measurement and frequency stability analysis," Proc. SPIE **10563**, 105633B (2017).
25. O. Lux, D. Wernham, P. Bravetti, *et al.*, "High-power and frequency-stable ultraviolet laser performance in space for the wind lidar on Aeolus," Opt. Lett. **45**, 1443–1446 (2020).
26. O. Lux, C. Lemmerz, F. Weiler, *et al.*, "ALADIN laser frequency stability and its impact on the Aeolus wind error," Atmos. Meas. Tech. **14**, 6305–6333 (2021).
27. F. Heine, K. Schieber, T. Meier, *et al.*, "High stability, fast tunable single frequency laser source for space based lidar applications," Proc. SPIE **10568**, 1056816 (2017).
28. F. Heine, R. Lange, S. Seel, *et al.*, "High stability lasers for lidar and remote sensing," Proc. SPIE **10567**, 105671E (2017).
29. H. Scheife, R. Lange, K. Schieber, *et al.*, "Frequency-stable seed laser for the Aeolus mission," Proc. SPIE **10566**, 105661M (2017).
30. S. W. Henderson, E. H. Yuen, and E. S. Fry, "Fast resonance-detection technique for single-frequency operation of injection-seeded Nd:YAG lasers," Opt. Lett. **11**, 715–717 (1986).
31. F. Trespidi, E. Stucchi, and E. Nava, "A novel cavity control technique for the stabilization of a burst, pulsed laser," Proc. SPIE **10567**, 105673O (2017).
32. T. Schröder, C. Lemmerz, O. Reitebuch, *et al.*, "Frequency jitter and spectral width of an injection-seeded Q-switched Nd:YAG laser for a Doppler wind lidar," Appl. Phys. B **87**, 437–444 (2007).
33. O. Lux, C. Lemmerz, F. Weiler, *et al.*, "Speckle noise reduction by fiber scrambling for improving the measurement precision of an airborne wind lidar system," *Conference on Lasers and Electro-Optics (CLEO)* Munich, Germany, June 23–27, 2019.
34. B. Witschas, C. Lemmerz, O. Lux, *et al.*, "Spectral performance analysis of the Aeolus Fabry–Pérot and Fizeau interferometers during the first years of operation," Atmos. Meas. Tech. **15**, 1465–1489 (2022).
35. F. Weiler, T. Kanitz, D. Wernham, *et al.*, "Characterization of dark current signal measurements of the ACCDs used on board the Aeolus satellite," Atmos. Meas. Tech. **14**, 5153–5177 (2021).
36. O. Lux, R. Reichert, C. Lemmerz, *et al.*, "CCD detector performance of the space-borne Doppler wind lidar ALADIN during the Aeolus mission," Appl. Opt. **63**, 6754–6775 (2024).
37. A. Cosentino, A. D'Ottavi, P. Bravetti, *et al.*, "Spaceborne lasers development for ALADIN instrument on board ADM-Aeolus ESA mission," Proc. SPIE **9626**, 96261U (2015).
38. W. Riede, P. Allenspacher, A. Ciapponi, *et al.*, "Qualification of laser optics for upcoming ESA space laser missions," Proc. SPIE **10564**, 105642K (2018).
39. N. Bartels, P. Allenspacher, W. Riede, *et al.*, "Removal of laser-induced contamination on ALADIN laser optics by UV/ozone cleaning," Proc. SPIE **11173**, 111731C (2019).
40. G. de Villele, J. P. do Carmo, K. Wallace, *et al.*, "ESA Atmospheric LIDAR (ATLID) testing, qualification, and calibration," Proc. SPIE **11852**, 118521J (2021).
41. G. S. Székely and F. Henzelin, "Design and qualification of the mechanisms for the ALADIN instrument," in *11th European Space Mechanisms and Tribology Symposium (ESMATS)*, B. Warmbein, ed. (2005), Vol. **591** of ESA Special Publication, pp. 85–90.
42. The Pierre Auger Collaboration, O. Lux and I. Krisch, "Ground observations of a space laser for the assessment of its in-orbit performance," Optica **2**, 263–272 (2024).
43. O. Reitebuch, C. Lemmerz, O. Lux, *et al.*, "Initial assessment of the performance of the first wind lidar in space on Aeolus," EPJ Web Conf. **237**, 01010 (2020).
44. G.-J. Marseille, J. de Kloe, U. Marksteiner, *et al.*, "NWP calibration applied to Aeolus Mie channel winds," Q. J. R. Meteorol. Soc. **148**, 1020–1034 (2022).
45. D. Wernham, A. Heliere, G. Mason, *et al.*, "Status of Aeolus-2 pre-development activities," *Aeolus 3rd Anniversary Conference*, Taormina, Italy, March 28–April 1, 2022.
46. A. Heliere, D. Wernham, G. Mason, *et al.*, "Status of Aeolus-2 mission pre-development activities," Proc. SPIE **12777**, 1277709 (2023).
47. EUMETSAT, "Towards EPS-Aeolus: facts and figures," EUMETSAT Brochure (2023), https://www.eumetsat.int/media/51304.
48. R. Chalex, L. Fiedler, T. Flament, *et al.*, "EUMETSAT EPS-Aeolus: status and outlook," *31st International Laser Radar Conference*, Landshut, Germany, June 23–28, 2024.
49. T. Flament, R. Borde, S. Joro, *et al.*, "Scientific activities at EUMETSAT for the proposed EPS-Aeolus programme," *31st International Laser Radar Conference*, Landshut, Germany, June 23–28, 2024.
50. S. Hahn, M. Bode, J. Luttmann, *et al.*, "FULAS: high energy laser source for future LIDAR applications," Proc. SPIE **11180**, 111805F (2019).
51. G. Ehret, P. Bousquet, C. Pierangelo, *et al.*, "MERLIN: a French-German space lidar mission dedicated to atmospheric methane," Remote Sens. **9**, 1052 (2017).
52. O. Reitebuch, Aeolus DISC consortium, and European Space Agency, "Challenges and achievements of ESA's Aeolus mission," *International Conference on Space Optics*, Antibes Juan-les-Pins, France, October 21–25, 2024.
53. A. Ciapponi, M. Porciani, D. Wernham, *et al.*, "Aeolus-2: status of pre-development activities," *31st International Laser Radar Conference*, Landshut, Germany, June 23–28, 2024.
54. O. Reitebuch, C. Lemmerz, E. Nagel, *et al.*, "The airborne demonstrator for the direct-detection Doppler wind lidar ALADIN on ADM-Aeolus. Part I: Instrument design and comparison to satellite instrument," J. Atmos. Ocean. Technol. **26**, 2501–2515 (2009).
55. C. Lemmerz, O. Lux, O. Reitebuch, *et al.*, "Frequency and timing stability of an airborne injection-seeded Nd: YAG laser system for direct-detection wind lidar," Appl. Opt. **56**, 9057–9068 (2017).

56. O. Lux, C. Lemmerz, F. Weiler, *et al.*, "Intercomparison of wind observations from the European Space Agency's Aeolus satellite mission and the ALADIN Airborne Demonstrator," Atmos. Meas. Tech. **13**, 2075–2097 (2020).

57. O. Lux, C. Lemmerz, F. Weiler, *et al.*, "Retrieval improvements for the ALADIN Airborne demonstrator in support of the Aeolus wind product validation," Atmos. Meas. Tech. **15**, 1303–1331 (2022).